UNIVERSITY OF THESSALY

SCHOOL OF ENGINEERING

DEPARTMENT OF MECHANICAL ENGINEERING

FATIGUE RESISTANCE OF WELDED T-JOINT CONNECTIONS MADE OF MILD AND HIGH STRENGTH STEEL FOR OFFSHORE APPLICATIONS

by

BILLIS D. ANTONIOS NIKOLAOS

MOURLAS K. CHRISTOS

Submitted in partial fulfillment of the requirements for the degree of Diploma in Mechanical Engineering at the University of Thessaly

Volos, 2024

Acknowledgements

We would like to sincerely thank everyone who contributed to the completion of this work. First, we would like to thank our thesis advisor Professor Spyros A. Karamanos, for his help and guidance during our studies and for collaboration in the Laboratory of Mechanics and Strength of Materials of the University of Thessaly. We also express our gratitude to him for giving us the opportunity to be members of his research team. We are also grateful to Professor Theocharis Papatheocharis for our excellent cooperation, support and guidance during the experimental procedure and assessment and the completion of this thesis. Also, we would like to thank Associate Professor Alexis Kermanidis for his help and collaboration in the Laboratory. Special thanks to PhD students Ilias Gavriilidis and Ioannis Goulas for their contribution to the completion of the numerical simulation, experimental procedure in the laboratory and for their valuable help.

Finally, but above all, we are grateful to our families and friends for their wholehearted love and support over the years. We dedicate this dissertation to our parents and sisters.

Abstract

Nowadays renewable energy offshore platforms have seen rapid growth in response to the lack of fossil fuels and a constant rise in temperature worldwide caused by the greenhouse phenomenon. These platforms provide sustainable sources while converting wind and wave energy to electrical energy. Floating wind turbines with special arrangements for wave energy exploitation, such as REFOS platform, have already made a breakthrough and their installation will soon be established in many deep-water locations in Europe. Harsh environmental conditions though, threaten these large-scale structures, impose them on extreme loading regimes and make them prone to corrosion. The multi-purpose platform constitutes the basis for the SIRENES project and is the subject of experimental investigation in the present thesis. SIRENES research project aims to ensure structural integrity and performance of the steel platform and improve offshore engineering by providing cost-effective alternatives.

The current study investigates the high cycle fatigue resistance of fillet welded T-joint connections made of mild steel (S355) and high-strength steel (S700), under four-point bending in room conditions. During the experiment, we monitored stiffness reduction and used magnetic particle inspection (MPI) to visualize crack initiation across the weld toe throughout the load cycles. Moreover, the use of finite element analysis gave us insights into the critical regions in order to have a more visualized picture of stresses distribution. The analysis of fatigue performance will enhance our understanding of potential cost and weight benefits of using high-strength steel in offshore platforms, such as Refos. The experimental data are presented along with graphs and photos at important stages.

Future ideas are proposed aiming at enriching the SIRENES targets and providing valuable data with numerical models for corrosion environments. Beyond the structural perspective of REFOS, a reduced fabrication cost is desirable to make more feasible its production and global establishment.

Table of Contents

List of Figures

List of Tables

List of Diagrams

Chapter 1: Introduction

Nowadays, the global energy matter is something that has not been fully solved yet, but many steps towards that assessment are being taken. Sustainable and renewable sources are the key factors for a wholly transformation with offshore renewable energy platforms emerging and gaining international attention. As fossil fuels are the first hope for producing energy environmentally friendly, offshore renewable energy projects, particularly wind farms, have attracted significant attention due to their capacity to utilize plentiful, clean, and renewable energy sources, including wind and wave energy. At the moment, the second most popular source is wind energy, as the leader is hydropower. Offshore wind energy offers a range of advantages over onshore wind energy, primarily by preventing deforestation, which is something that must be avoided in order to extend as much as possible the lifetime of the earth. In addition, far from sore, more consistent and more powerful wind can be found and also visual pollution is minimized with no spatial restrictions for the size of the wind turbines. However, this means that the structural integrity of these platforms becomes vital for their long-term viability and performance as they can be much bigger from the onshore platforms. Today, most wind farms are made up of bottom-fixed wind turbines. These structures have seen considerable progress, contributing to the development of large-scale wind farms. However, research around this type of turbine has reached a limit. Additionally, many countries lack shallow coastal areas, making the construction of these farms in these regions economically infeasible due to the significant influence of sea depth on project costs. Although it remains at an early phase of development with no physical applications yet, an ideal solution to this problem could be a fully floatable wind turbine and can produce electricity not only from the wind, but also from the wave. Since 2007, various models and designs of floating wind turbines have been tested in the open sea with or without rough conditions [1]. Researchers and engineers have been working to overcome challenges, improve cost-effective methods, and enhance the durability and lifespan of components of the structure, as the open ocean tends to apply higher loads and more fatigue damage compared to shallow water where traditional bottom-fixed turbines are based. In 2023, the first operational floating platform that generates up to 2MW energy was connected to the grid 2 miles away from coastal coast of Spain (DemoSATH project) [1]. Creating an effective design for a floating structure that guarantees structural integrity while minimizing costs marks a substantial progress in current technology and expands the possibilities of wind energy.

This proposal introduces a model concept of floating platforms that will offer a breakthrough at the existing offshore wind technology [2]. A multi-functional floating Tension-Leg-Platform (TLP) steel system, REFOS (2016-2019), is a project that combines wind and wave energy exploitation. It reaches a very high score in producing the maximum energy output and economies of scale by using wind energy through the wind turbine (WT) and wave power through cylindrical Oscillating Water Column (OWC) equipment. (Figure 1a).

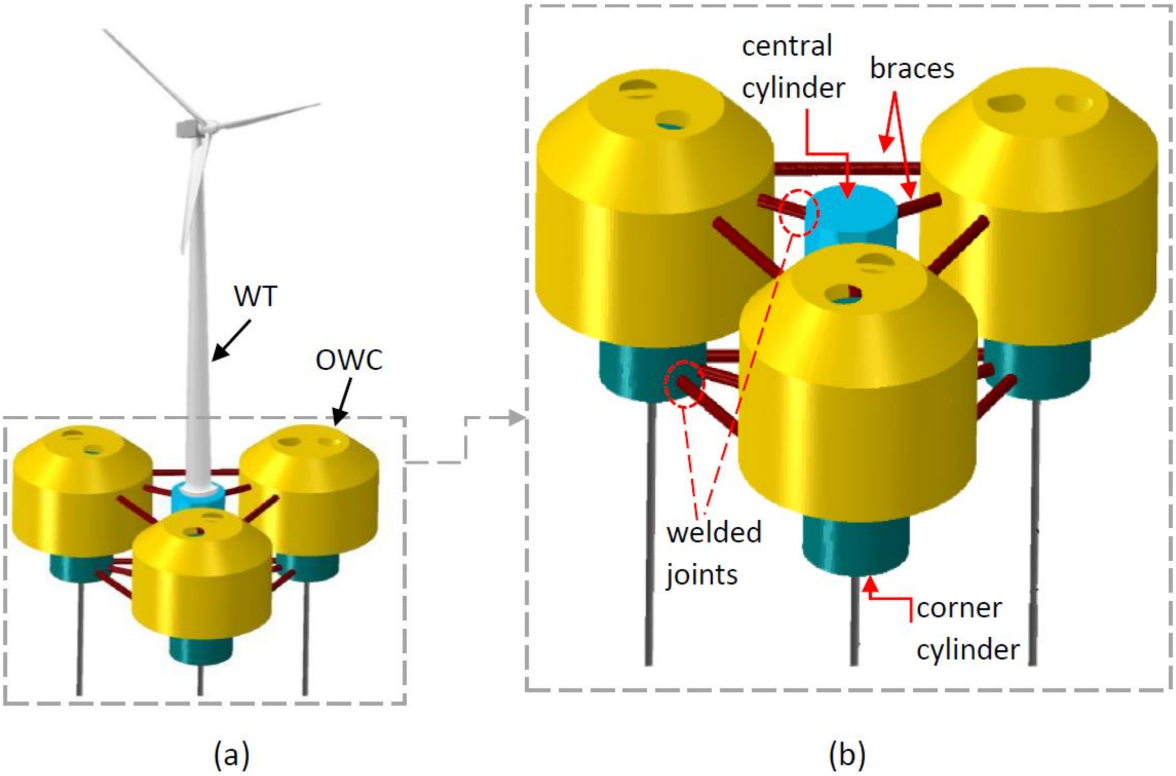

Figure 1: (a) Configuration of REFOS (b) parts of the triangular platform that specimens were extracted for experiments

Refos platform is the key factor of this research project named SIRENES. This initiative focuses on enhancing the structural performance and integrity of the platform, with the goal of advancing this concept to a level that meets as much as possible the demands of industrial applications. The SIRENES project is dedicated to improving the structural integrity of offshore floating systems, thereby emerging cost-effectiveness with wind and wave energy in oceanic environments [3]. This initiative is based on previous research efforts, aiming to enhance the structural performance of a deep-water floating system. The platform's steel components are vulnerable to corrosion and experience repeated elastic deformations as a result of climate change. The ultimate goal is to elevate the technological readiness of the offshore platform, making it physically acceptable for industrial applications. The present thesis addresses the second phase of the SIRENES project, which includes the preparation and testing of the materials and steels that comprise the braces [4]. Considering the large dimensions of the platform shown in Figure 1, it is clear that real experiments can only be conducted by developing a sufficiently scaled-down model and results can be acceptable with the necessary changes.

1.1 Purpose of thesis

A platform that floats in open sea, such as REFOS, is consistently subjected to complex and dynamic loading conditions, making the study of fatigue behavior a crucial aspect of their design and reliability assessment and remains the basic concern of investigation in this thesis. For structural components, especially in marine environment where corrosion is a big enemy for every kind of material, fatigue failure is a common concern, making it even more important when wind, waves and currents impose cyclic loads. Welded joints, cylinders and steel braces (Figure 1b), that compose the TLP platforms, are the 'hot-spots' where the maximum load is concentrated [5]. Understanding the fatigue performance of structural materials is crucial for ensuring the long-term durability and safety of offshore floating wind turbines.

This research focuses on experimental investigation of fatigue resistance of welded T-joint connections. These are located on the main structural braces that connect the Oscillating Water Column (OWC) with the Wind Turbine (WT) and on the stiffeners that enhance the structural integrity of OWC [6]. For the braces, full-penetration weld is used and for the stiffeners is preferred fillet-weld joints. In addition, this proposal compares the behavior in two distinct steel grades: S355, commonly used structural steel, and S700, a high-strength steel, with or without post-weld treatment known as High-Frequency Mechanical Impact (HFMI).

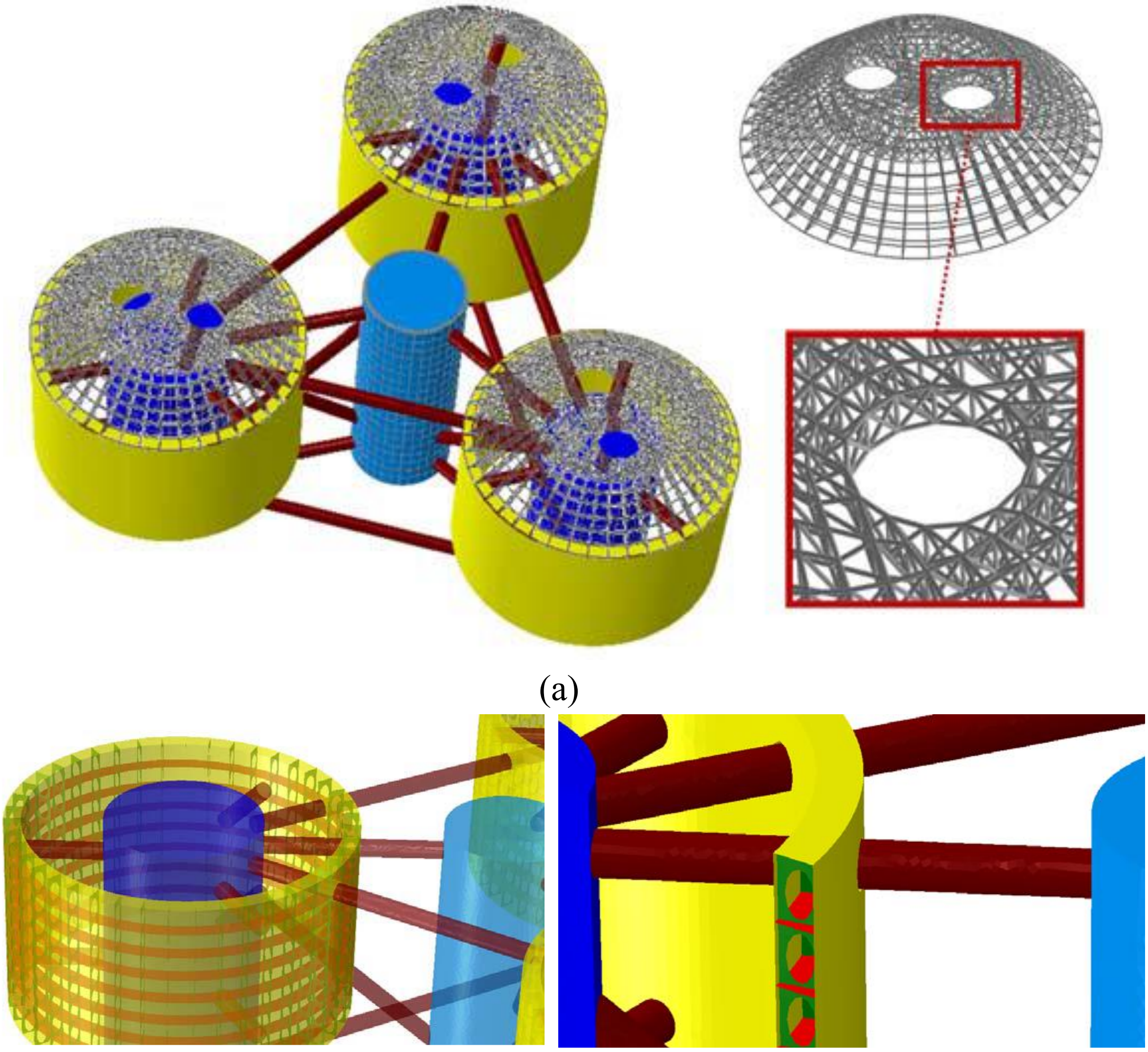

(a)

(b) (c)

Figure 2: (a) 3D truss structure for the support of OWC cup, (b) and (c) stiffeners of OWC devices

S355 is widely employed in various structural applications and currently to the majority of offshore wind structures due to its favorable combination of strength, toughness, ductility and weldability. On the other hand, S700 represents a high-strength steel known for its enhanced mechanical properties, offering potential advantages in terms of weight reduction and increased structural efficiency. The objective of this study is to systematically analyze and compare the fatigue performance of these two steel grades and evaluate the employment of high-strength steel (HSS), providing valuable insights into their applicability for offshore floating wind turbine structures.

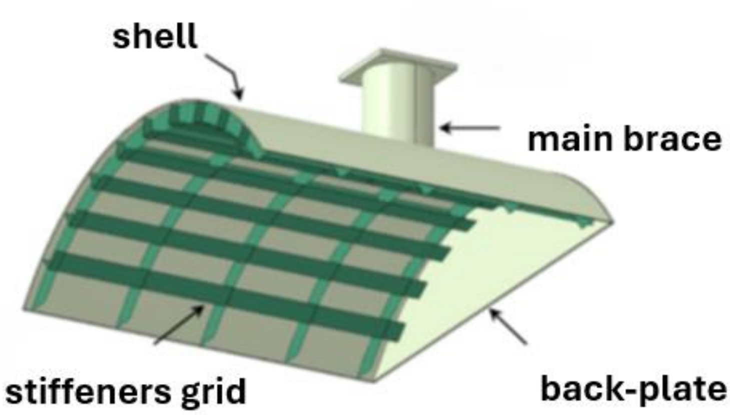

Figure 3: Numerical model of the welded specimens from experiments about ultimate strength and fatigue of stiffened tubular joints (shell and solid elements are shown with green and grey color, respectively)

The research methodology involves cyclic loading tests under 4-point bending (4PB) process. In this experiment, bending moment is applied on the region of the weld, where maximum stresses are found, representing the real full-scale structure design. Cyclic tests simulate the high-amplitude cyclic loading conditions typically associated with extreme events, such as storm conditions, while 4PB helps in acquiring data with minimum errors because of misalignments of the tested specimen. More specifically, the two different types of welding procedures will be compared in terms of life-cycle resistance across three specific applied stresses (50%, 75%, 91% of nominal yielding stress) along with the post-weld treatment of the two steel grades, S355 and S700. The experimental data obtained from these tests will be analyzed, with detailed graphs in Chapter 5, to understand the behavior under high cyclic fatigue.

1.2 Contribution of the present thesis

The primary objective of the present thesis is to conduct the deeper study and comparison of the welding types for each different material, which constitutes a key factor to the structural integrity of the floating platform REFOS, through experimental procedures. Regions of critical stress are the main concern, where the initiation of discontinuities or cracks may occur, potentially leading to the fracture of structural braces and stiffeners grid. The outcomes of this research aim to contribute to the development of advanced design guidelines and material selection frameworks for offshore floating wind turbine units.

Moreover, the findings will provide a detailed assessment of the performance and fatigue tolerance of steels under cyclic loading in air, while laying the theoretical groundwork for future investigations in corrosive environments (sea water). This study will further support the optimization of key trade-offs between material strength, durability, and weight, thereby enhancing the overall efficiency and reliability of these innovative renewable energy systems in challenging offshore conditions. Additionally, it will address the application of high-strength steel (HSS) in offshore structures, recognizing its potential to improve structural resilience, cost-effectiveness, sustainability, and the performance of offshore energy platforms.

1.3 Dissertation layout

A brief outline of the following chapters is presented below:

- Chapter 2 presents the fundamentals of the experiment details, including theory of fatigue life, 4-point bending, material properties, welding types and post-treatment method
- Chapter 3 refers to a simulated point of view model of T-joint specimens using ABAQUS
- Chapter 4 explains the method of the experiment in depth detailing (coupon preparation, equipment used, procedure)
- Chapter 5 outlines the results and outcomes of the tests, focusing on the total cycles that each specimen completed until failure, and comparing the start-to-finish change of the stiffness
- In the last chapter, Chapter 6, the emphasis shifts towards suggestions and subsequent actions that can improve the analysis and support a thorough underwater investigation and numerical assessment.

Chapter 2: Theory Overview

2.1: Fatigue

Fatigue resistance of welded steel tubular connection is one of the key features for the structural integrity of the platform. To be more specific, hot-spot stresses are the main factor impacting fatigue life at critical locations, such as the weld-toe. In the fatigue experiments, the specimen is subjected to a variable load with a constant mean stress σ_m and a constant stress amplitude σ_a, where:

$$\sigma_m = \frac{\sigma_{max} + \sigma_{min}}{2}, \qquad \sigma_a = \frac{\sigma_{max} - \sigma_{min}}{2}$$

Finally, the number of loading cycles, N_f, under which the specimen fails (fractures) is determined.

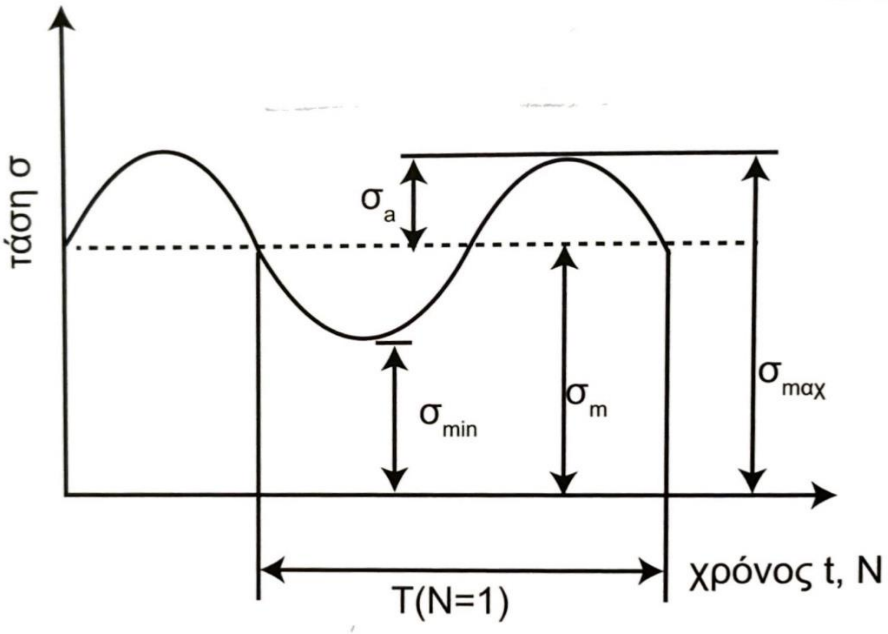

Figure 4: Represents a sinusoidal load function, N is a cyclic load and T is a period. The frequency can be determined by the function $f = \frac{1}{T}$

High cycle refers to fatigue experiment where failure occurs between 10^3 and 10^6 to 10^7 cycles (region II). If the experiment surpasses this range of cycles, it is deemed to have achieved its fatigue endurance limit and is classified as a run-out.

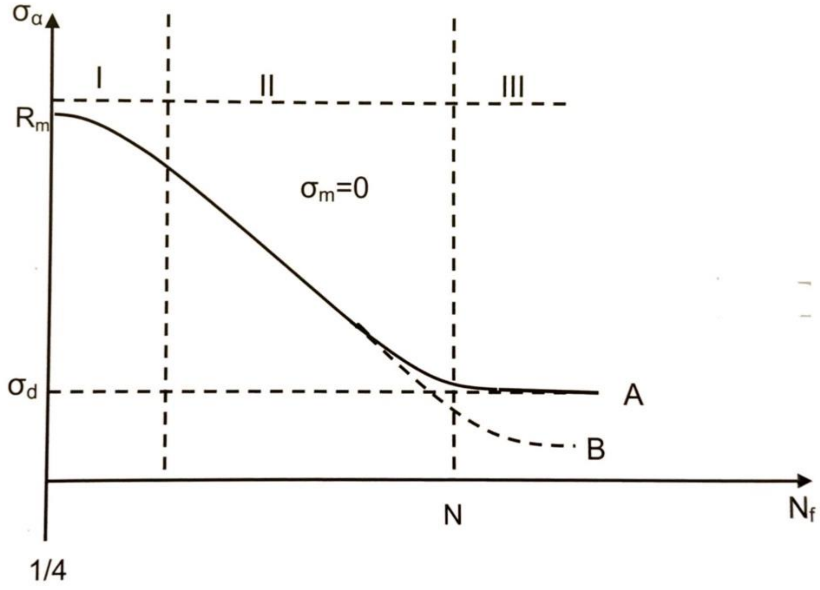

Figure 5: WOHLER curve for σ_m=0 but can also be determined experimentally for every σ_m, is a graphical representation of cycles in relation with applied stress. This graph is divided in three regions. The first (I) is the low cycle fatigue where the specimen will fail after a relatively low count of cycles because of the high stresses. The second region (II) is the high cycle fatigue and the third region (III) where the stresses are low can describe the endurance limit of the material.

Another important factor is the stress Factor, which is set to R=0.5 in all of our experiments

$$R = \frac{\sigma_{min}}{\sigma_{max}}$$

As the fatigue test progresses, surface cracks develop on the weld toe and defects in the heat-affected zone. The crack growth rate is dependent to the material, the applied load and the number of cycles as shown in the diagram below.

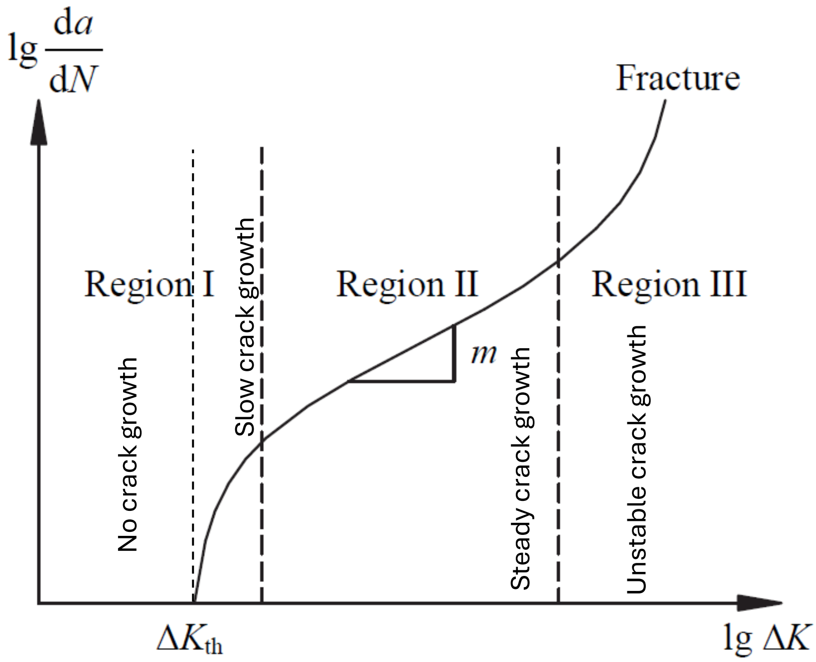

Figure 6: graphical representation of crack growth ($\frac{da}{dN}$) in relation to stress intensity factor (ΔK) on a log-log scale.

As these cracks get bigger most of the mechanical properties of the specimen change. [7]

2.2: Material properties

After the analysis of experimental data, the mild steel (S355) showed a yield strength (σ_y) from 350 to 366 MPa, an ultimate tensile strength (σ_{uts}) between 487 and 495 MPa and necking was observed at strain 17.2-19%. Combining that information, we conclude that s355 is mild steel incorporating strength, ductility and weldability making it suitable for various structural uses. S700 on the other hand is a high-strength steel. After testing, it achieved a much higher yield strength between 715-835 MPa and ultimate tensile strength between 823-868 MPa. However, the trade-off of increasing strength is reduced ductility, as indicated by its lower elongation necking at strain 5.7-10%. Overall, S700 is a high-strength steel well-suited for structures where maximum strength and minimum deformation is required.

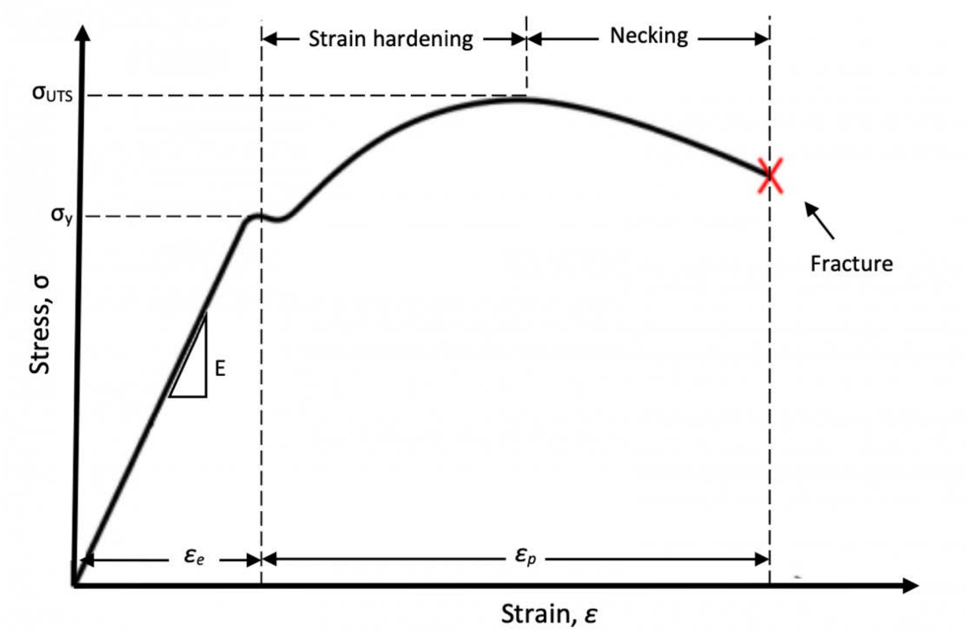

Figure 7: Stress- Strain diagram.

For S355 steel the orientation has a relatively minor impact on its mechanical properties. The differences in yield strength, ultimate tensile strength, and elongation between the longitudinal and transverse directions are small, with less than a 5% difference. This indicates that S355 is relatively isotropic in nature, meaning its mechanical properties are fairly uniform regardless of the direction of the applied load.

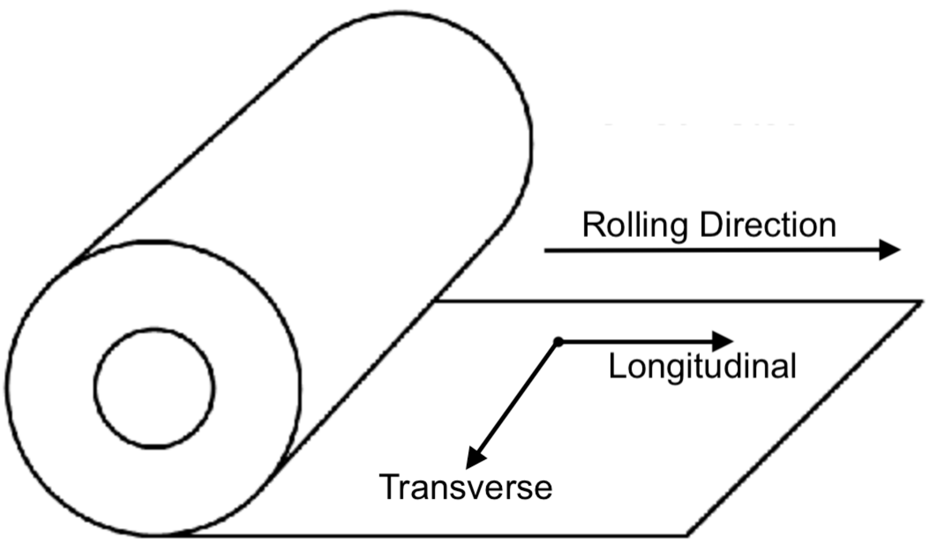

Figure 8: Material's orientation with regard to rolling direction

In contrast, the anisotropic behavior is significantly stronger in S700 high-strength steel. The yield strength and ultimate tensile strength are higher in the transverse than in the longitudinal orientation, whereas the ductility is lower. More precisely, compared to the longitudinal direction, S700 where yield strength reaches 746 MPa, Ultimate Tensile Strength goes up to 827 MPa and 7.4-10% elongation at necking. In the transverse direction shows a yield strength up to 835MPa and 5.7-7.5% elongation at necking. This would suggest that, although S700 was stronger in the transverse direction, it was less ductile and less able to resist plastic deformation prior to failure.

Ratcheting behavior-so named because it describes the progressive development of plastic strain during cyclic loading is orientation dependent. The longitudinal specimens on S700 exhibits a more ductile behavior and higher cycle hardening compared to the transverse specimens while on S355 we observe a completely different behavior on the orientations [8]

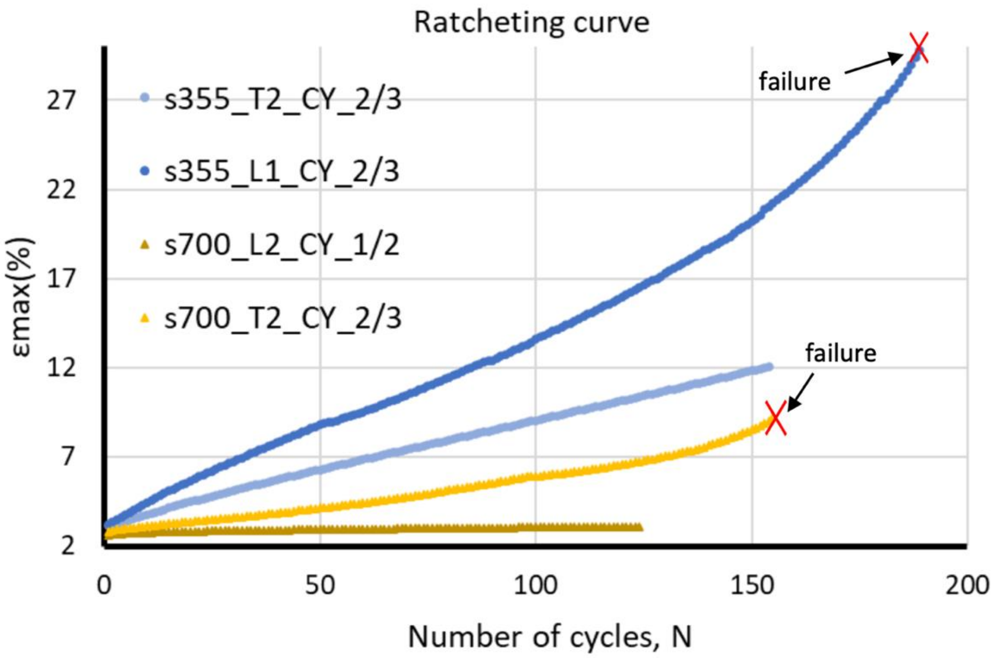

Figure 9: Ratcheting curves for S355 and S700 steels

S700			
DIRECTION	σ_{uts} (MPa)	σ_{yield} (MPa)	E_{neck}%
LONGITUDINAL	823-827	715-746	7.4-10
TRANSVERSE	855-876	805-835	5.7-7

Table 1: S700 material properties

S355			
DIRECTION	σ_{uts} (MPa)	σ_{yield} (MPa)	E_{neck}%
LONGITUDINAL	486-489	346-362	17.6-19
TRANSVERSE	487-495	357-366	17.2-18.2

Table 2: S355 material properties

2.3: 4 point bending theory

Researchers who wish to analyze the behavior of a specimen under bending force choose different types of procedures in order to have the desired results depending on their needs. In this experiment, the most appropriate way to apply bend load on the T-joint model is 4-point bending (4PB).

There are several reasons why 4PB can offer the best possible results to this experiment. Before that, let us identify what kind of method this is.

At first, bend is a complex sittuation for a beam. It is consisted of both tension and compresion with a neutral axis separating these two phenomenons. In our case, the upper surface of the model suffers from tesion and the lower surface from compresion (in contrast with figure 11). Together, they combine a bending moment.

In a 4-point bending experiment a beam or, in our case, a T-shape specimen is placed under two rolling supports (F_0 and F_3) that can withstand heavy treatment. Then, load is applied to the beam from two other rolling supports (F_1 and F_2) that are located in between and facing the other direction (upwards) as shown in figure 10. They can also resist heavy-duty applications and lengths a_1 and a_2 are even.

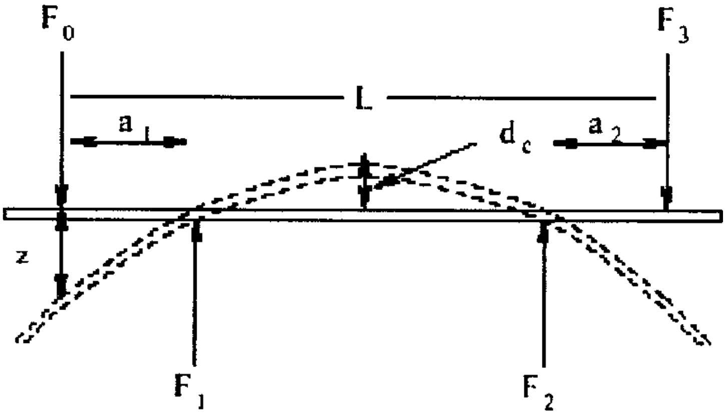

Figure 10: 4-point bending on a free body diagram view

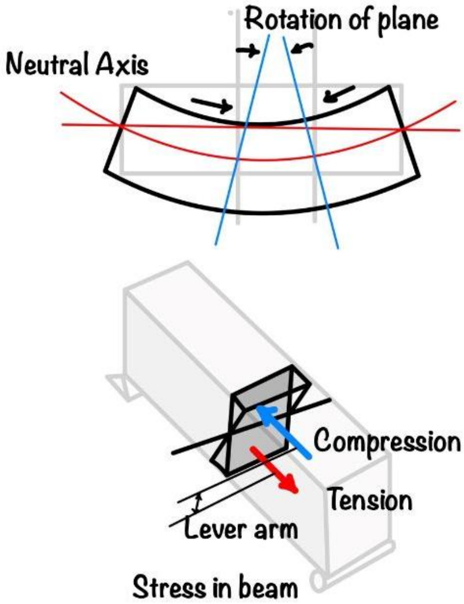

Figure 11: 3D view of a beam with applied bending moment

As a result, the inner part of the beam ($L-a_1-a_2$) is put to a ‘pure’ bend and takes the shape of an arc, as shown in the figure above.

Unlike three-point bending, which centers the maximum stress at a single spot, four-point bending generates a constant stress region across the width of the specimen between the two loading supports. Also, the shear stress in this region is zero, as shown in the pictures. This is a key factor in the research world because this uniformity helps in collecting valid information more easily. Specifically, when executing an experiment, the adjustments of the specimen before the start must be as precise as possible for the purpose of receiving accurate data. Sometimes the measurements are invalid because of the human factor – 0.5 mm (for this test) is enough to bring wrong results. That is why 4PB is helpful. This uniform stress region allows a more consistent and reliable assessment of material properties like flexural strength and stiffness, which are vital factors for any kind of experiment. To conclude, it ensures that the observed behaviors are due to the material itself rather than experimental errors as it reduces sensitivity to specimen misalignment. [9]

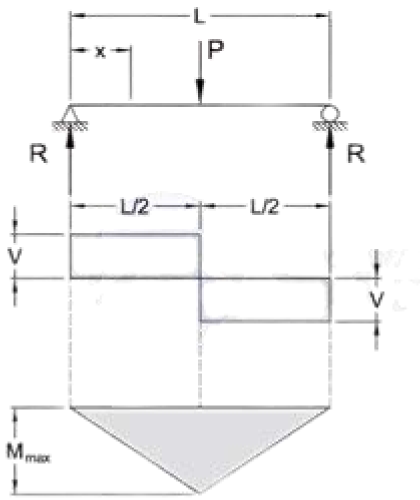

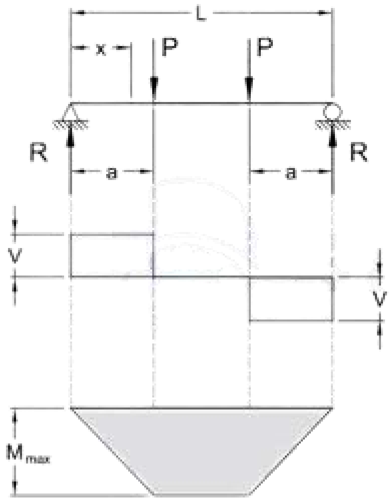

(a) (b)

Figure 12: (a) 3-point bending and (b) 4-point bending on free body diagram with shear force and bending moment diagram

2.4: Welding methods

Fillet weld

This is the most common type of welding method as it takes the minimum execution time compared with other more complex methods. It joins two metal plates together, such as a T-joint specimen shown in Figure 13, at a 90-degree angle. The weld creates a triangular cross-section, filling the gap between the steel plates by adding the welding metal (in this case the same material as the plates).

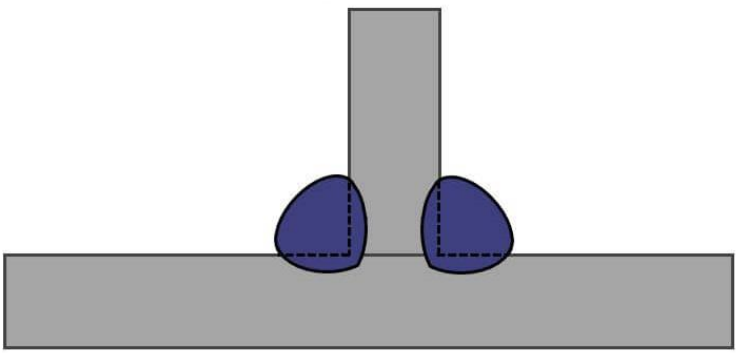

Figure 13: fillet weld

Full penetration

The industry prefers to use full penetration welding to achieve maximum strength from a welded structure. This method is more durable, especially in fatigue resistance, due to the uniformity and completeness of the weld and the fact that the thickness of the material is fully penetrated. For instance, on a T-shape joint, the edges of the vertical plate get beveled to form a V shape. Then, this part and the horizontal one are held in place together so that the welding metal will be applied in the space that the V is making. This combination is responsible for the much better resistance in fatigue (and not only). [10]

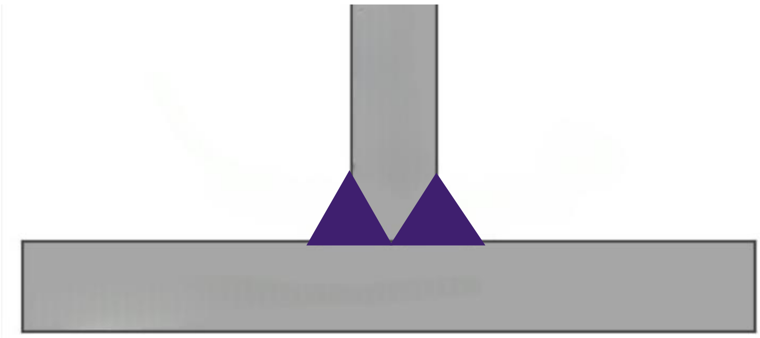

Figure 14: full-penetration weld

In addition, while full penetration weld is more durable from the fillet weld, there are ways that a structure can become even stronger. After completing a full penetration weld, by applying post-weld treatment, the overall durability of the model can be increased by 2 to 10 times more. One of the most common treatments is High-Frequency Mechanical Impact (HFMI).

High-Frequency Mechanical Impact treatment, also known as hammer or needle peening, is a cost-effective method for enhancing the durability of welded components. This method focuses on eliminating the majority of local residual stresses that have formed during the welding and that could initiate a crack quicker. HFMI also smoothens the sharp corners, grooves and other discontinuities caused also by the welding procedure and that could be catastrophic for the material, as these small openings could make a crack open much more rapidly. As a result, this procedure enhances fatigue life for the specimens as it prevents crack initiation and increases local hardening. [11]

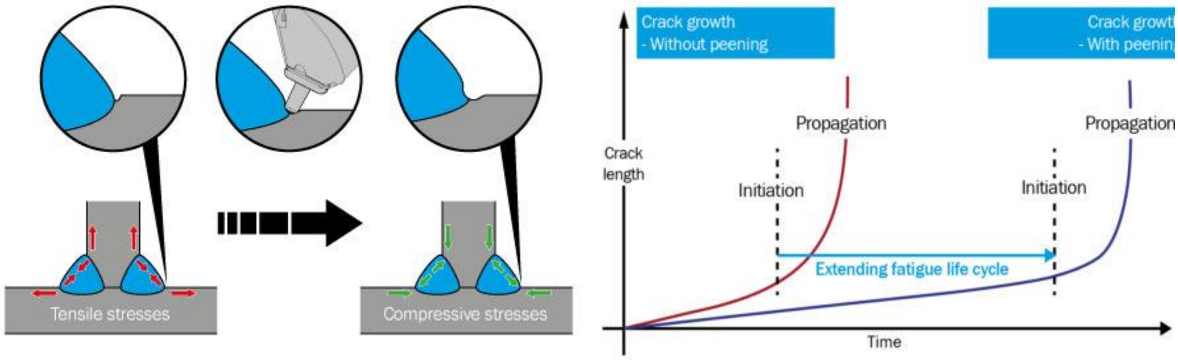

(a) (b)

Figure 15: (a) stresses across the weld toe before and after peening process, (b) crack propagation ratio with and without peening

2.5: Magnetic Particular Inspection

MPI stands for Magnetic Particle Inspection. It's a non-destructive method used to inspect surface defects and cracks without damaging the specimen. This method works by magnetizing the specimen with an external AC electromagnet yoke, that creates a magnetic field. That magnetic force when it encounters a discontinuity, secondary magnetic poles are created which attract the magnetic particles. To enhance that procedure, we used the black and white method, where the tested area is sprayed with a white contrast paint, followed by the application of a black paint that consists of ferrous particles to define the defects. [12]

(a) (b)

Figure 16: (a) MPI ink and white contrast paint, (b) magnetic yoke

Chapter 3: FEA

3.1: Introduction to the method

Prior to conducting the experiments, we wanted to have a visual representation of how the specimen would respond under the four-point bending, identifying where the maximum stresses would occur, and at which point the specimens fail. To achieve this, a plain-strain two-dimensional elastic-plastic model was created using Abaqus.

3.2: Procedure

Firstly, the specimen along with the diameter of the rollers and the exact distances was measured carefully. Following this, a 2D model of the t-shape was created as a deformable solid (steel), with the rollers as rigid wire.

Afterward, the assembly was created by positioning the rollers in the desired locations. Next, the mesh was generated using quadrilateral structured elements.

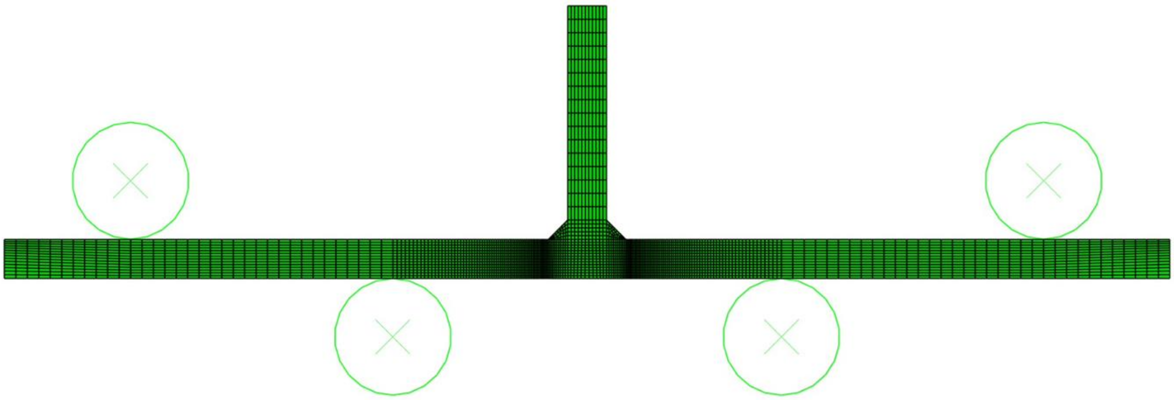

Figure 17: Assembly and mesh on abaqus

The model was dividing in rectangular areas and two triangular to facilitate mesh generation. In critical areas where higher accuracy was required, such as near the weld toe, the mesh is refined, while in non-critical areas the mesh density was reduced for lower computational cost.

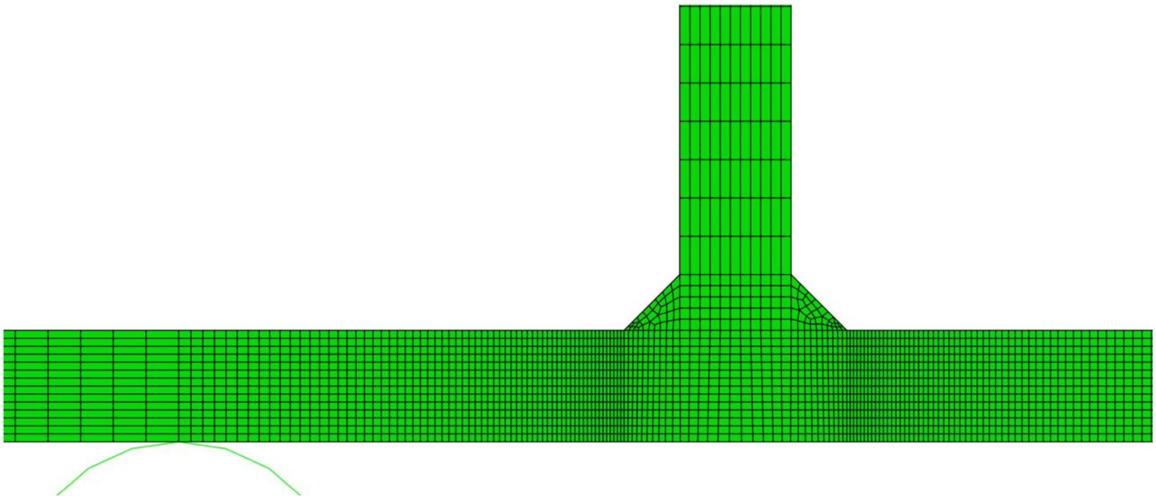

Figure18: Zoomed mesh on abaqus

Then the material properties were defined to simulate the behavior of high strenght steel S700.The material parameters were set as following: yield stress of 700MPa, Young's modulus of 210 GPa and Poison's ratio of 0,3.

Based on experimental data, we assumed that the behavior of S700 could be modeled as a perfect plastic material.

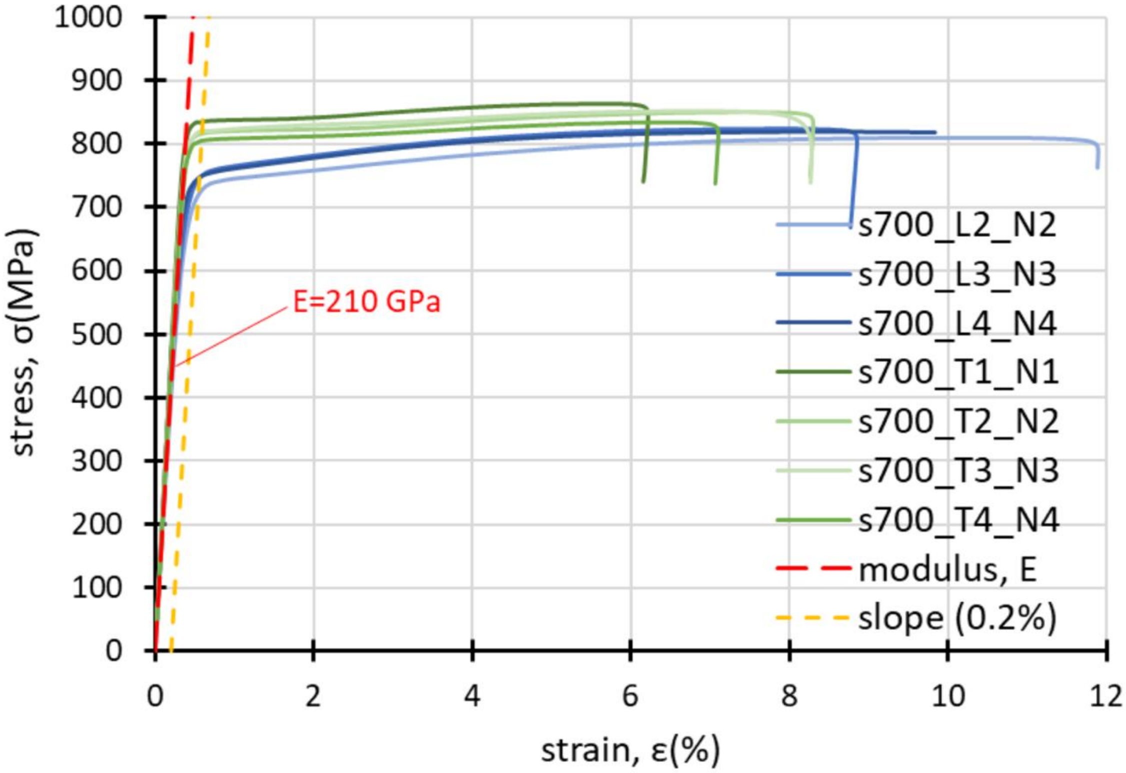

Figure 19: Stress-strain curves of high-strength steel S700

Finally, the boundary conditions and loading scenarios were applied to accurately represent the experimental setup. The top rollers were anchored, and the bottom rollers were displaced upwards by 1mm.

3.3: Results

The results of the finite element analysis aligned with our expectations. The maximum stresses were concentrated close to the middle of the specimen, with a significant increase at the locations where the geometry transitions. This behavior highlights the critical areas that are most vulnerable to failure under loading conditions.

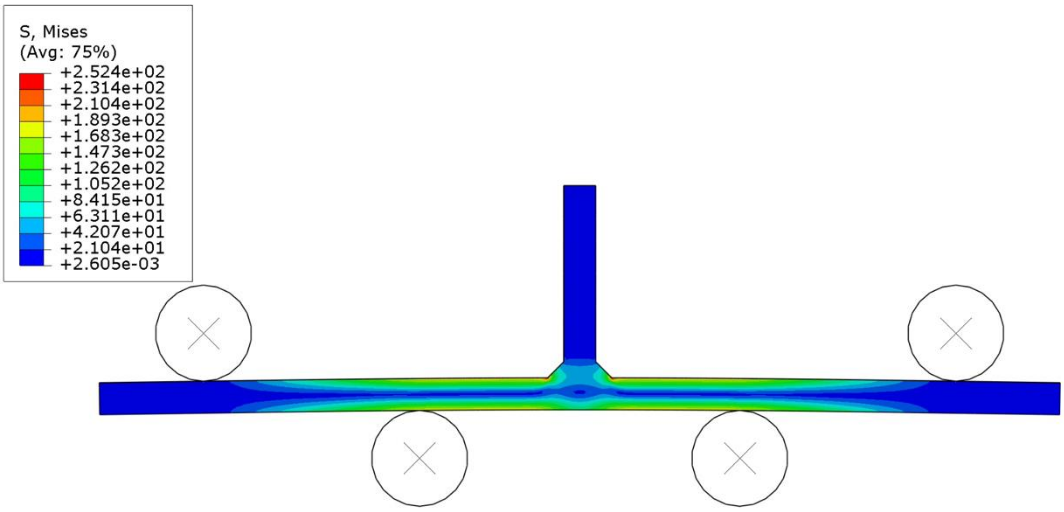

Figure 20: Mises stress distribution for 1mm displacement

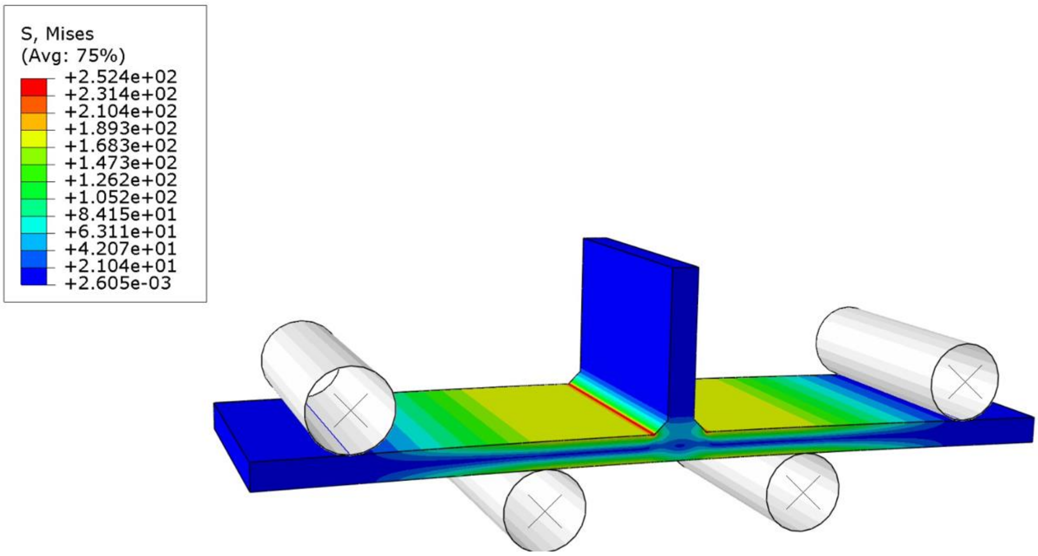

Figure 21: Mises stress distribution for 1mm displacement (3D)

By using the extrude function we can have a 3D representation of our simulation

For displacement 1mm reaction force on each roller is $\frac{F}{2} = 49.2232$ N per mm so applied force is 9.8445 KN

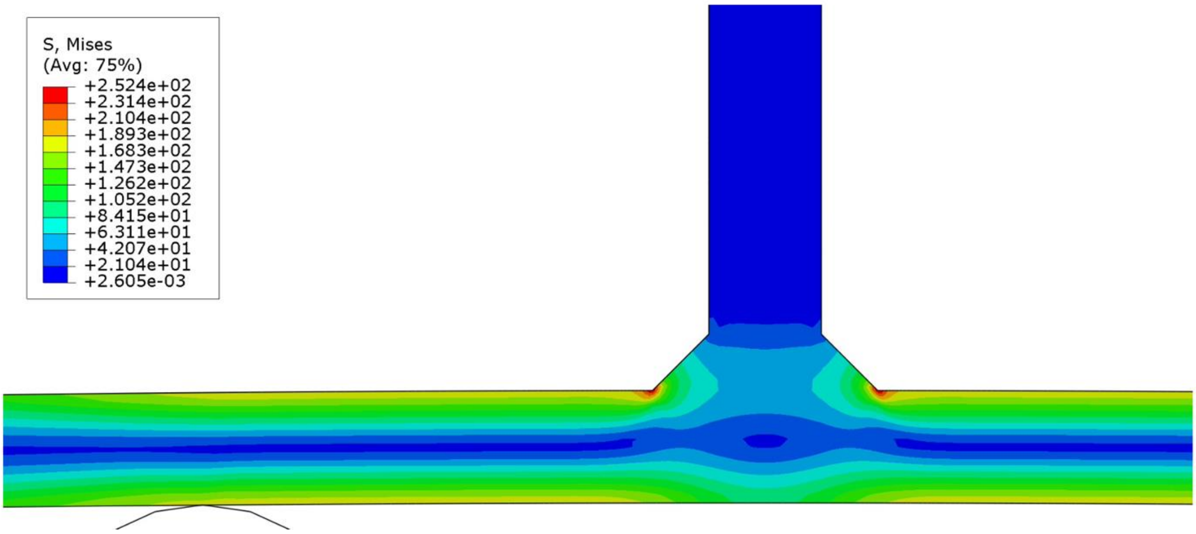

Figure 22: Mises stress distribution for 1mm displacement (zoomed)

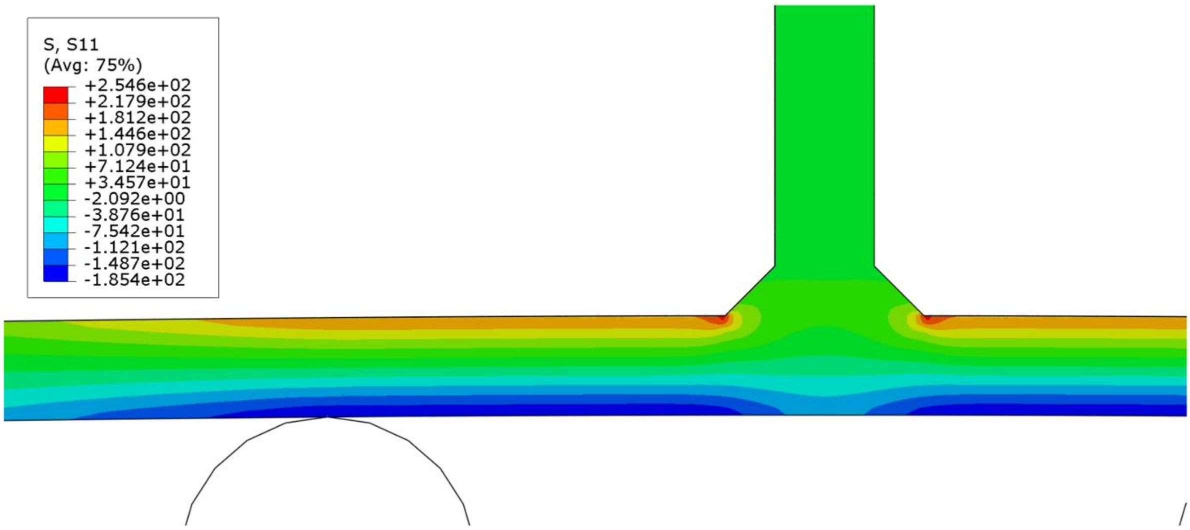

Figure 23: σ_{xx} stress distribution for 1mm displacement

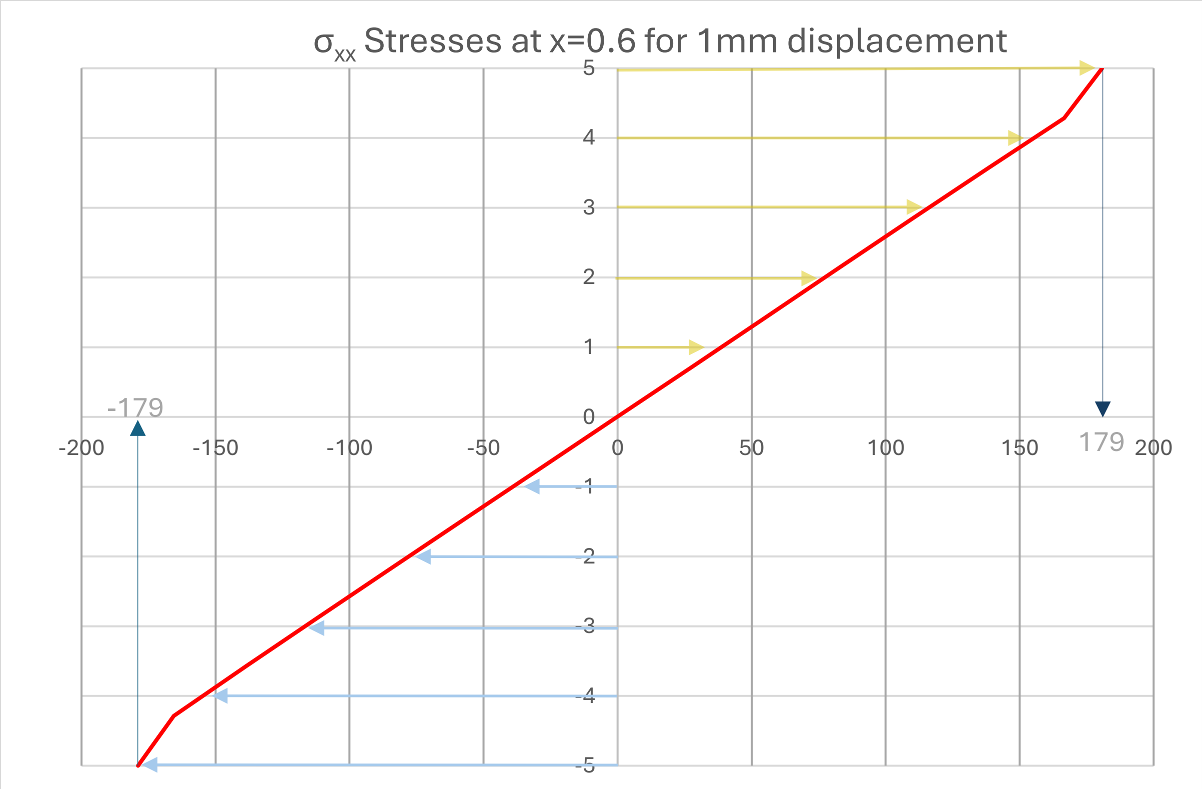

Diagram 1: σ_{xx} Stresses at x=0.6 for 1mm displacement

As previously stated in the four-point bending theory, FEA confirmed that the top side is under tension and the bottom side is under compression.

Chapter 4: Experimental method

4.1: Coupon preparation

The specimens under investigation are made of two steel plates, each with a thickness of 10 mm welded in a T-shape form as shown below, manufactured by VETA S.A..

The geometric measurements of all the specimens are identical and correspond to the SIRENES proposal.

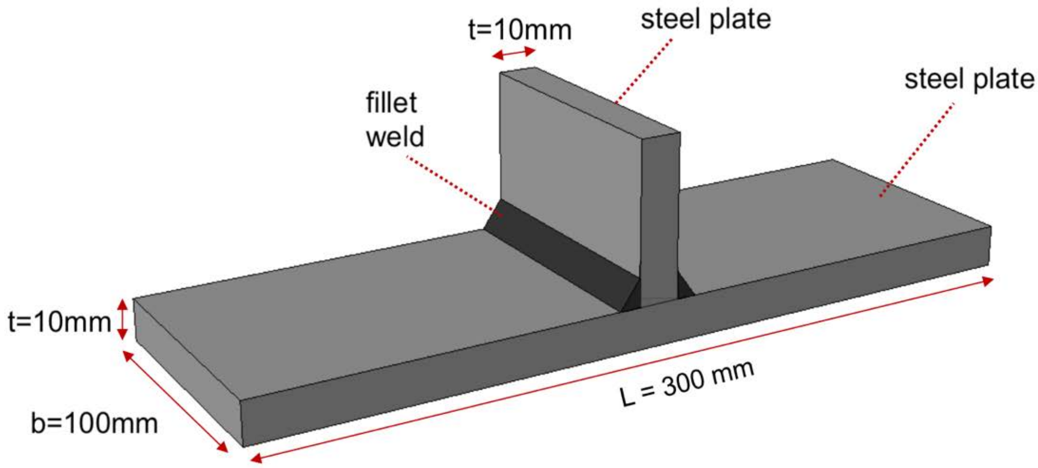

Figure 24 :Specimen geometry and dimencions

Furthermore, the specimens were measured with a ruler and marks were made with a marker to help us locate the center and the four points that the rollers should touch so the expirement is calibrated.

Finally we color the specimen with white contrast paint so its easier to identify the crack initiation with the use of MPI method.

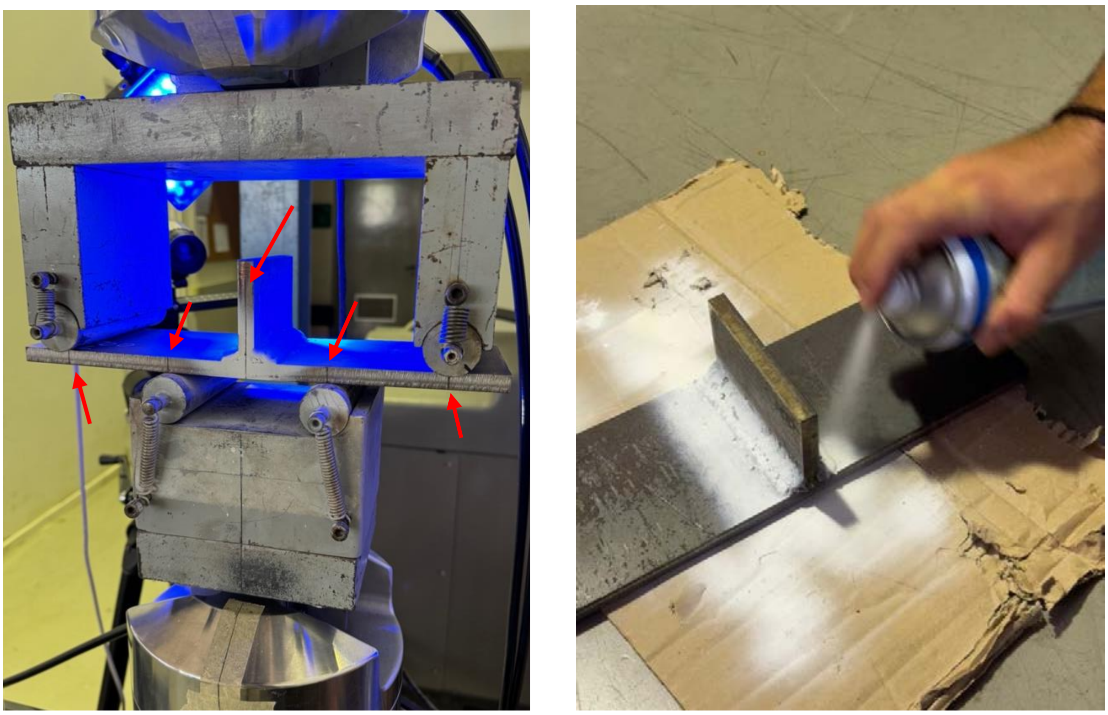

(a) (b)

Figure 25: (a) The experimental setup, with the specimen positioned at the desired location using the alignment marks (indicated by red arrows)

(b) Spraying procedure

(c) experimental and camera setup

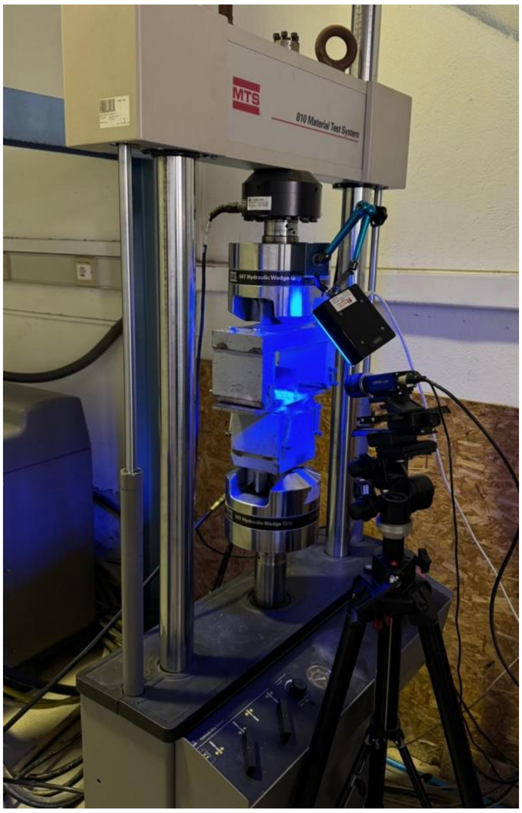

(c)

4.2: Equipment

All the experiments were conducted in the laboratory of Mechanics, strength of Materials, Department of Mechanical Engineering at the University of Thessaly. The fatigue tests have been performed in an MTS 318.10 loading frame with a force capacity up to 100kN powered by an MTS SilentFlo 505.11 which employs an MTS FlexTest SE digital controller. Besides that, we use a LIMESS camera on a tripod combined with a blue light setup to capture the crack initiation as well as the crack propagation. Finally, to perform the magnetic particle inspection, we used the MAGNAFLUX model Y1 in conjunction with white contrast color spray and black MPI ink spray.

4.3: Procedure

Firstly, the machine was warmed up by completing some cycles without any load. Secondly, we attached the support fixtures to the center of the claps by performing the necessary measurements. After that, we positioned the specimen in the precise location so everything was aligned.

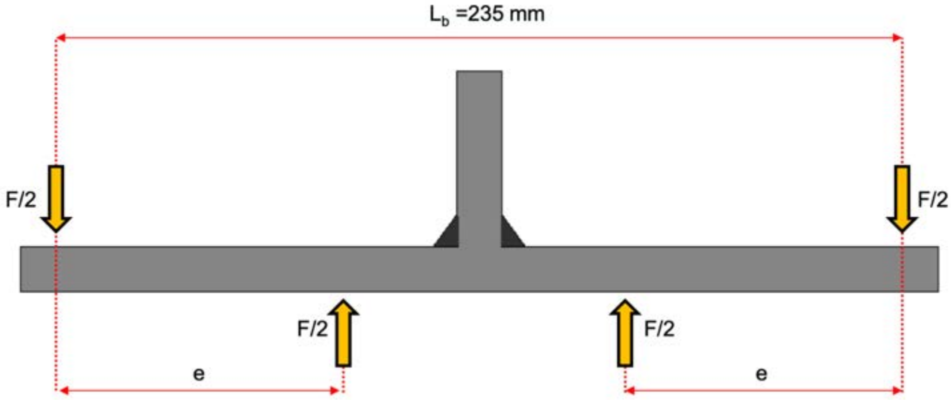

Figure 26: sketch of the experimental setup with applied forces

In the next step, we calculated the force based on the selected percentage of the yielding stress for testing. We tested three specific percentages (50%, 75%, and 91%). We believe that this range of loads is appropriate to give us a pretty good overview of each material behavior. To calculate the applied forces, we measured the bending moment arm (e) which is equal to 67.5 mm and converted them to nominal stresses. That conversion was first done by hand, solving the problem analytically using the bending stress formula

$$\sigma = \frac{M}{I} \cdot y_{max}$$

In this equation, I is the moment of inertia of the cross-section in beams which is calculated by the following formula

$$I = \frac{1}{12} \cdot b \cdot h^3$$

Where $b = 100mm$ and $h = 10mm$ as shown in the figure above y_{max} is the perpendicular distance to the neutral axis. In our case $y_{max} = 5mm$,

σ is the nominal stress and M is the bending moment. The bending moment is calculated by the method of sections, where each section is analyzed as a free-body diagram using the equilibrium equations (ΣF_x=0, ΣFy=0, ΣM=0). With that procedure the moment diagram is created.

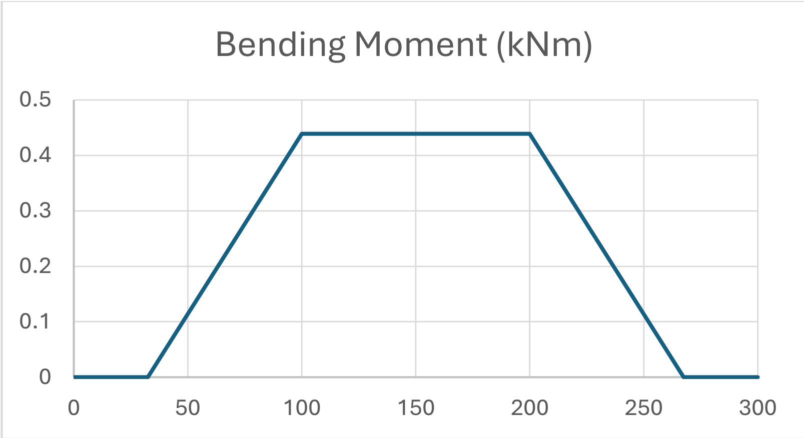

Diagram 2: bending moment diagram across the length of the specimen

In the following experiments that process was automated with the use of Excel.

Load to stress					Stress to load			
b	=	100	mm		b	=	100	mm
h	=	10	mm		h	=	10	mm
W	=	1,667E-06	m^3		W	=	1,667E-06	m^3
α	=	67,5	mm		α	=	67,5	mm
P	=	13	kN		σ	=	519,5	MPa
M	=	0,439	kNm		M	=	0,866	kNm
$σ_y$	=	355	Mpa		$σ_y$	=	700	MPa
σ	=	263,3	Mpa		P	=	25,7	kN
percentage	=	74,2	%		percentage	=	74,2	%

Figure 27: screenshot of the excel stress-force calculator

Chapter 5: Experimental results

specimen	load amplitude, ΔP (kN)	P_{max} (kN)	$\sigma_{nom, max}$ (MPa)	cycles to failure, n_f
Fillet Weld				
TJ-355_1	8.0	16.0	324 (0.91 $\sigma_{nom, y}$)	1,098,877
TJ-355_2	6.5	13.0	263 (0.75 $\sigma_{nom, y}$)	2,731,701
TJ-355_3	4.4	8.8	178 (0.50 $\sigma_{nom, y}$)	4,000,000 (run out)
TJ-700_1	15.8	31.6	640 (0.91 $\sigma_{nom, y}$)	87,923
TJ-700_2	12.85	25.7	525 (0.75 $\sigma_{nom, y}$)	294,300
TJ-700_3	8.65	17.3	350 (0.50 $\sigma_{nom, y}$)	1,143,695
Full Penetration Weld				
TJ-355_1	8.0	16.0	324 (0.91 $\sigma_{nom, y}$)	1,734,000
TJ-700_1	15.8	31.6	640 (0.91 $\sigma_{nom, y}$)	99,800
Full Penetration Weld HFMI treatment				
TJ-355_1	8.0	16.0	324 (0.91 $\sigma_{nom, y}$)	2,707,600
TJ-700_1	15.8	31.6	640 (0.91 $\sigma_{nom, y}$)	209,070

Table 3: experimental data results

5.1: Fillet welded specimens

5.1.1: s355

Sample 2 (91% of $\sigma_{nom, max}$):

This was the first sample that was put to the test, as sample 1 was used to execute a pilot test. It contributed to calibrating the machine, adjusting the specimen to the precise location, and applying a monotonic load to ensure that the resistance and yield limit matches the theoretical analysis.

The following table shows the characteristics of this experiment:

specimen	ΔP (kN)	P_{max} (kN)	$\sigma_{nom, max}$ (MPa)	$R = P_{min}/P_{max}$	cycles to failure, n_f
S355_s2_fl	8.0	16.0	324	0.5	1,098,877

During the experiment, we acquired data that when plotted, the following diagram was created. Axial load (in kn) and axial displacement (in mm) are adequate to describe the behavior of the specimen during the test. By dividing these two pieces of information, the stiffness of the T-joint can be calculated which, as expected, is decreased across the whole process. In other words, the deviation of the slope of each cycle and the total displacement (ratcheting) eventually will drop. On the right of the diagram, the number of cycles is presented.

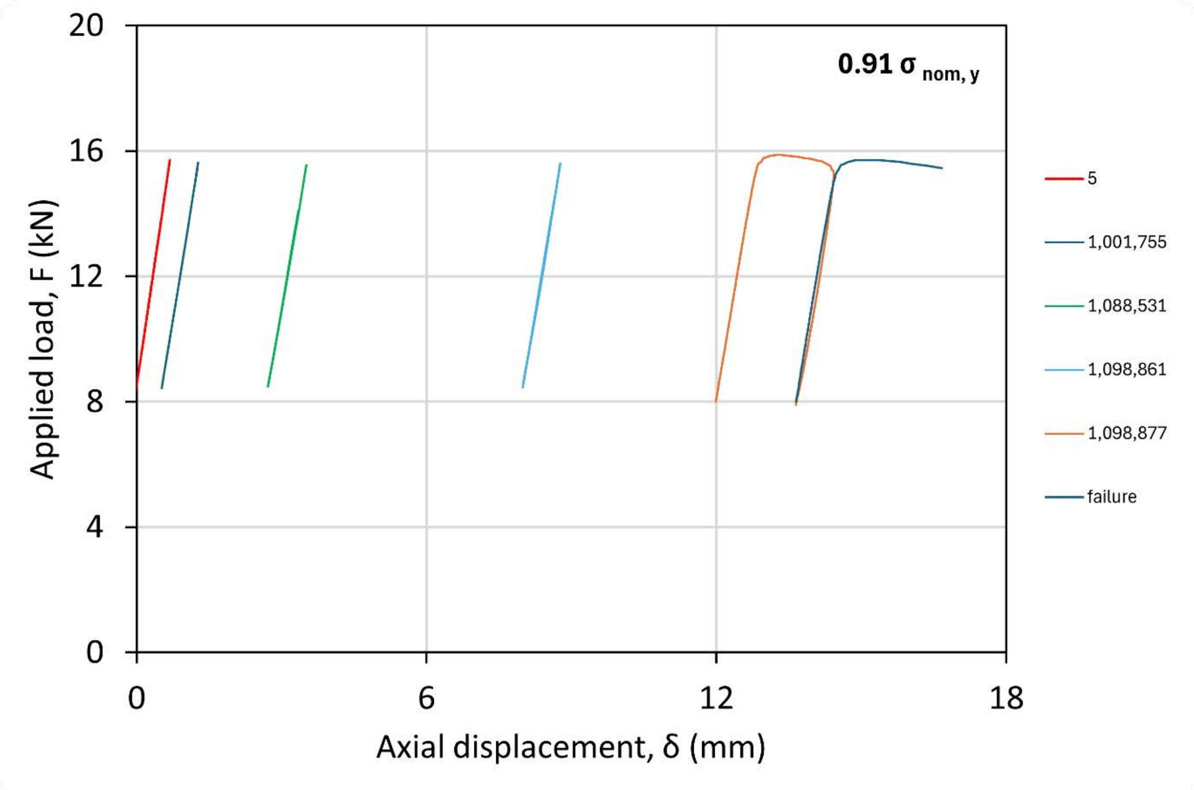

Diagram 3: Load-displacement curves under cyclic loading at specific load stages S355 fillet specimens

3,900 cy

(a) L-side

(b) R-side

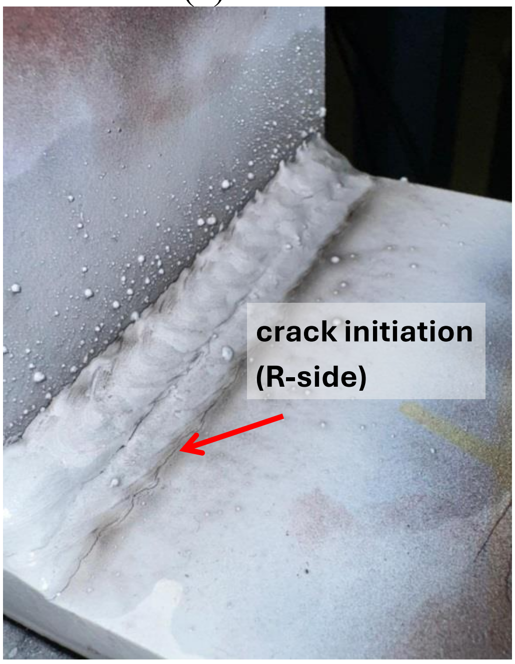

6,000 cy

(c) L-side

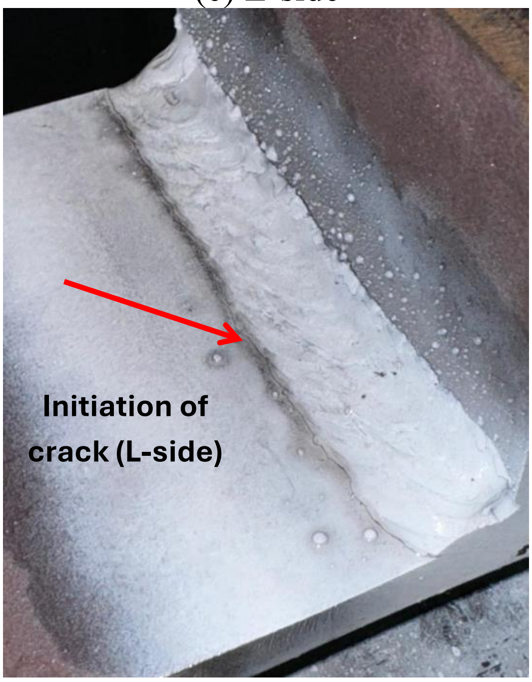

650,000 cy

(d) L-side

(e) R-side

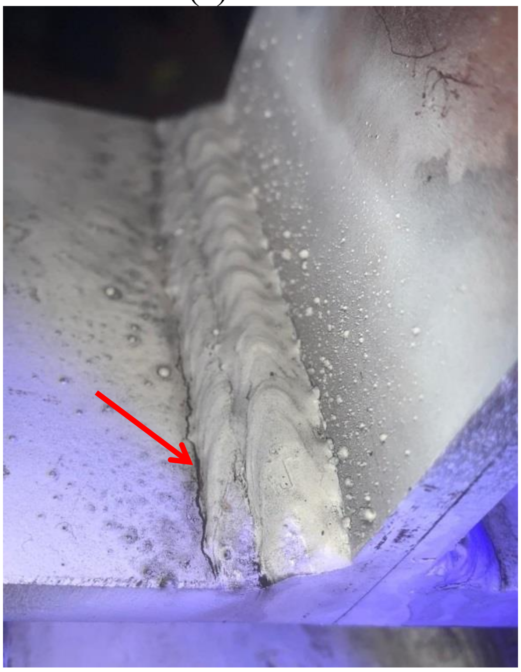

1,050,000 cy

(f) R-side

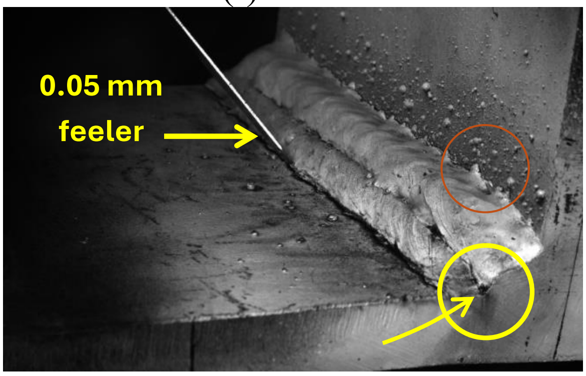

1,070,000 cy

(g) R-side

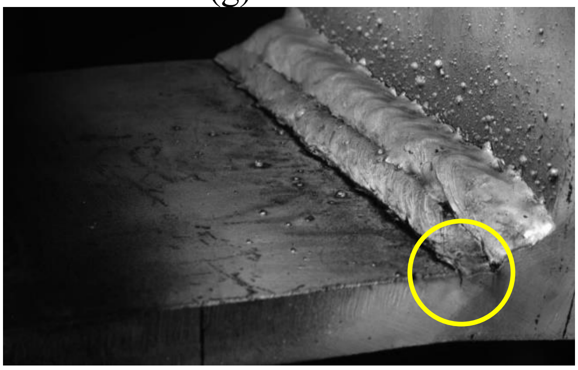

1,098,877 cy - failure

(h)

(i)

(j)

Figure 28: Fatigue crack development at the weld toe for specimen S355_s2_fl under cyclic loading at 91% $\sigma_{nom,\ yield}$ (arrows indicate detected cracks). (a-j)

While the experiment was ongoing, the model was photographed and comments were made on what was observed. More specifically, on the right side the crack initiated at cycle 3,900, as on the left side this occurred at cycle 6,000. After 1,000,000 cycles of nonsignificant changes, the crack began to propagate rapidly and the opening was at least 0,005 mm (tested with a feeler). Finally, the axial load couldn't reach the P_{max} input of 16 kn after 1,098,877 cycles, which meant the failure of the model.

Sample 3 (75% of $\sigma_{nom, max}$):

The following table shows the characteristics of this experiment:

specimen	ΔP (kN)	P_{max} (kN)	$\sigma_{nom, max}$ (MPa)	$R = P_{min}/P_{max}$	cycles to failure, n_f
S355_s3_fl	6.5	13	263	0.5	2,731,701

The diagram that follows shows the behavior of this steel during the experiment. The maximum applied load is 75% of the yielding load and the stiffness decrease is also visible between the first and the last cycle (the column on the right of the diagram)

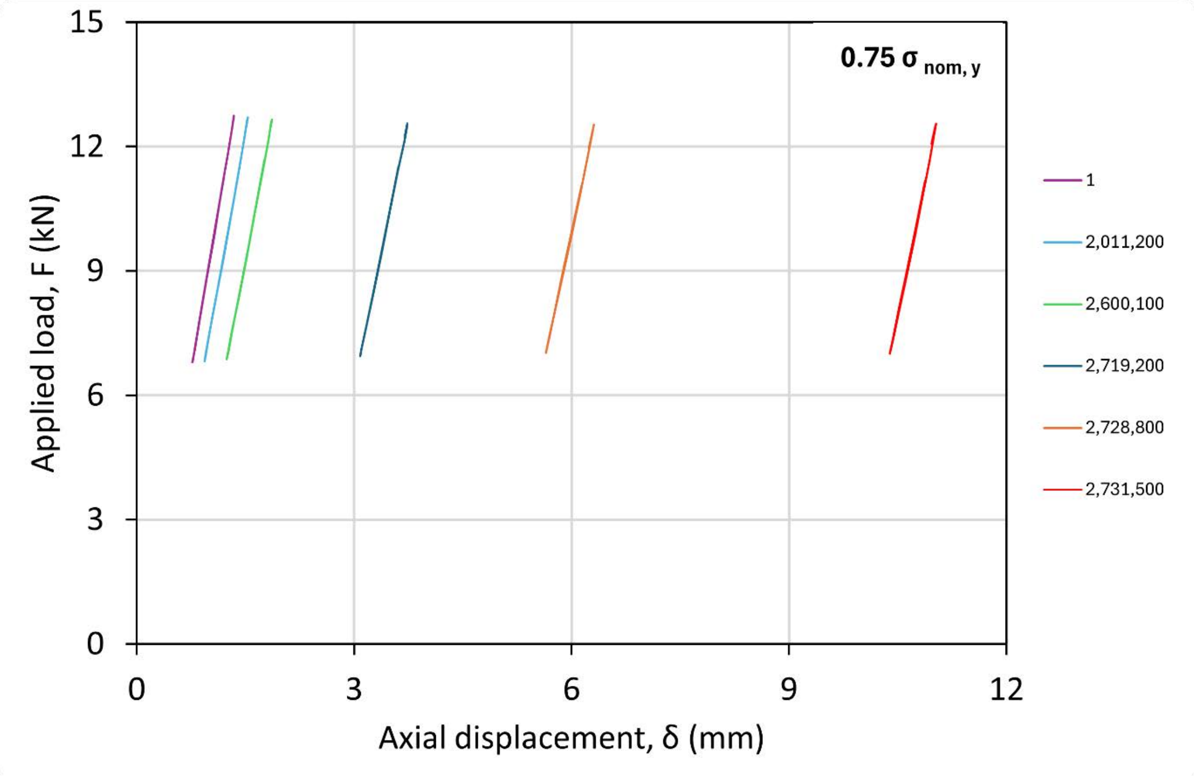

Diagram 4: Load-displacement curves under cyclic loading at specific load stages S355 fillet specimens

1st cy (a)

102,500 cy (b)

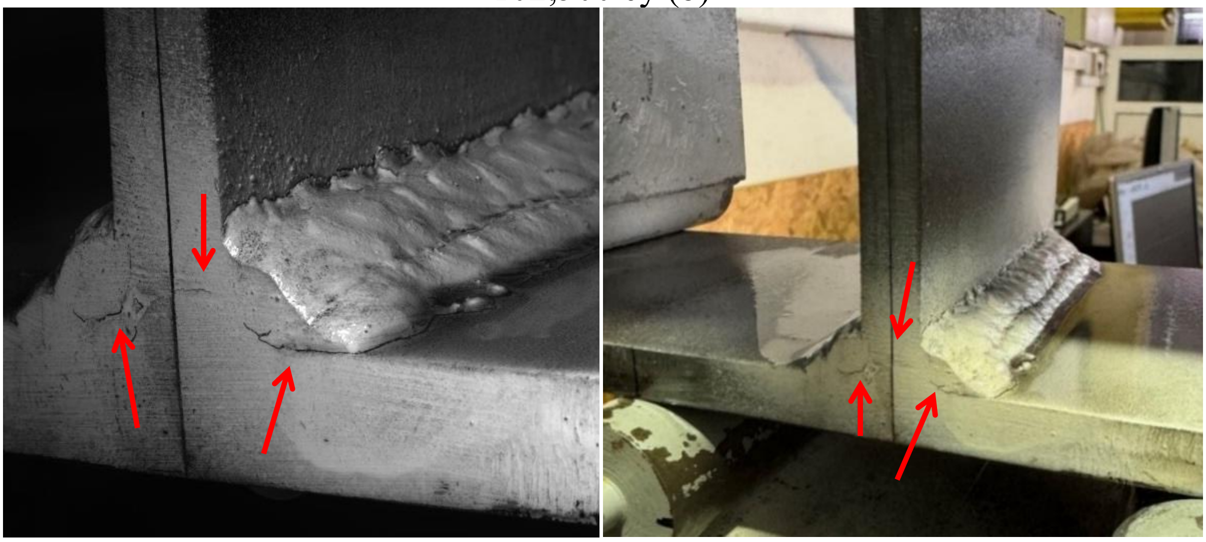

430,000 cy (c)

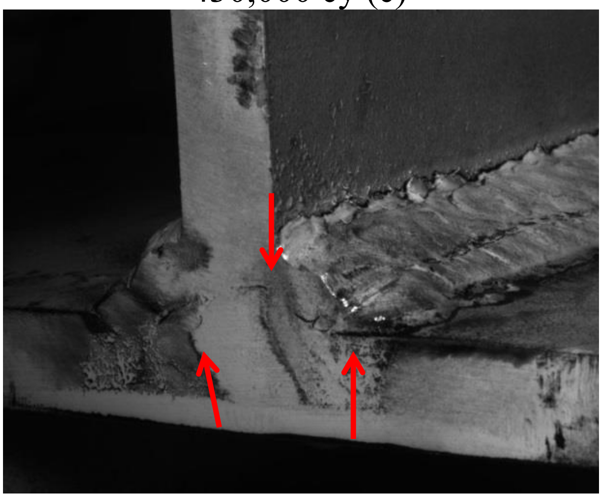

978,000 cy (d)

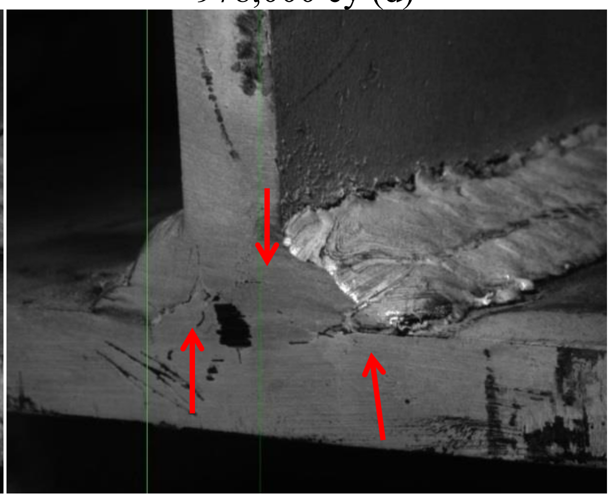

1,570,000 cy (e)

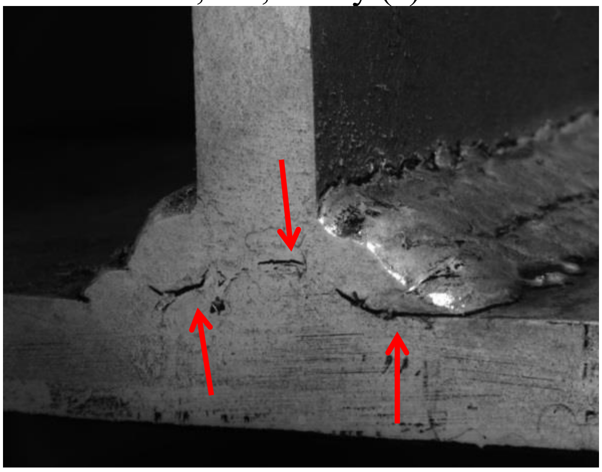

2,011,200 cy(f)

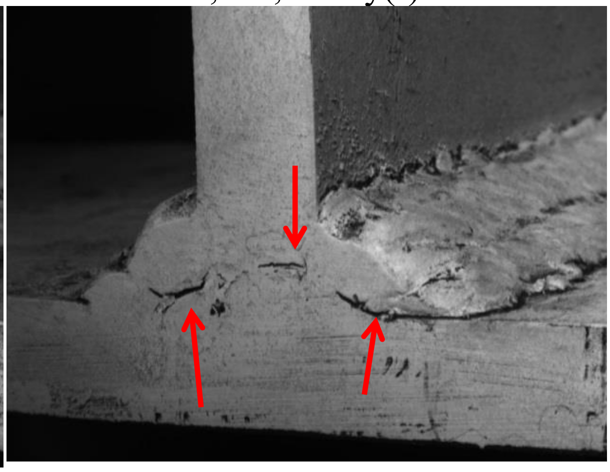

2,541,000 cy (g)

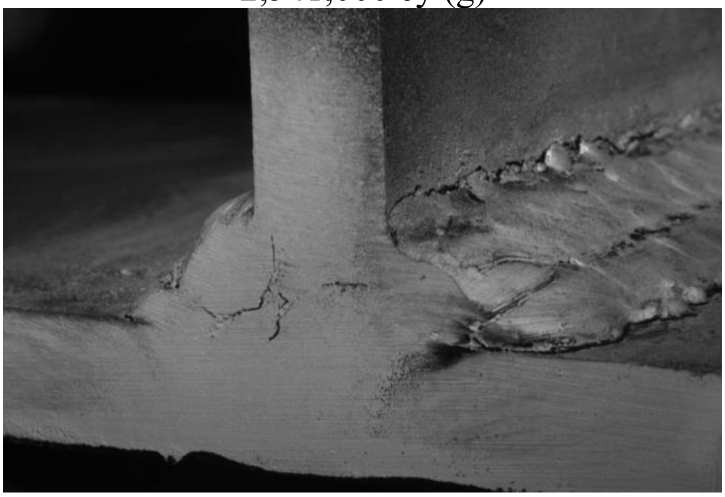

2,650,200 cy (h)

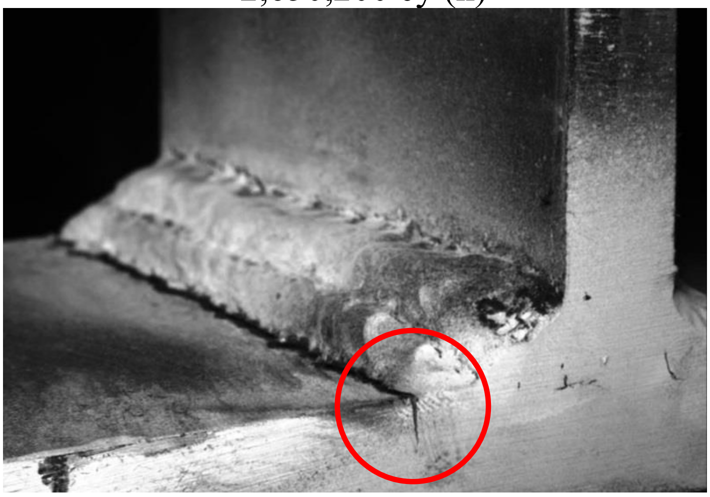

2,731,701 cy – failure

(i)

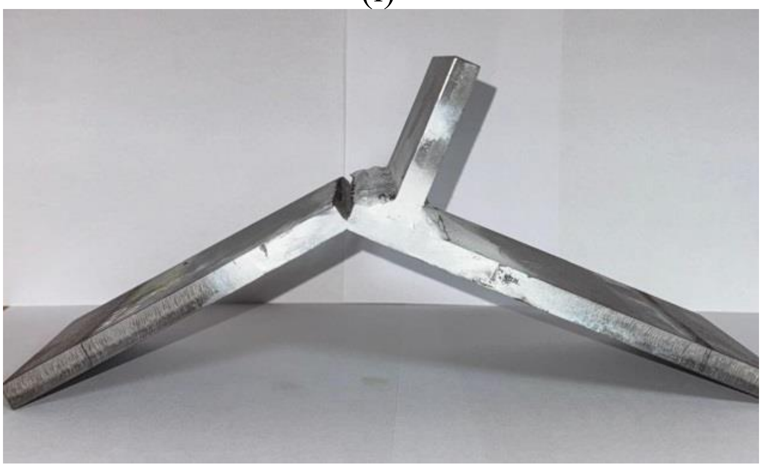

(j)

Figure 29: Fatigue crack development at the weld toe for specimen S355_s3_fl under cyclic loading at 75% $\sigma_{nom, yield}$ (arrows indicate detected cracks). (a-j)

After repeating the Magnetic Particle Inspection (MPI) at cycle 102,500, the crack has already begun to appear. The red arrows mark the rupture that occurred on the face of the specimen. Throughout the test, there are no significant changes in the rate at which the crack propagates when, after 2,600,000 cycles, the opening has reached the full width of the model. At that moment, the material is weak and approaches its failure. This specimen failed after 2,731,706 full cycles.

Sample 4 (50% of $\sigma_{nom, max}$):

The following table shows the characteristics of this experiment:

specimen	ΔP (kN)	P_{max} (kN)	$\sigma_{nom, max}$ (MPa)	$R = P_{min}/P_{max}$	cycles to failure, n_f
S355_s4_fl	4.4	8.8	178	0.5	4,000,000 (run out)

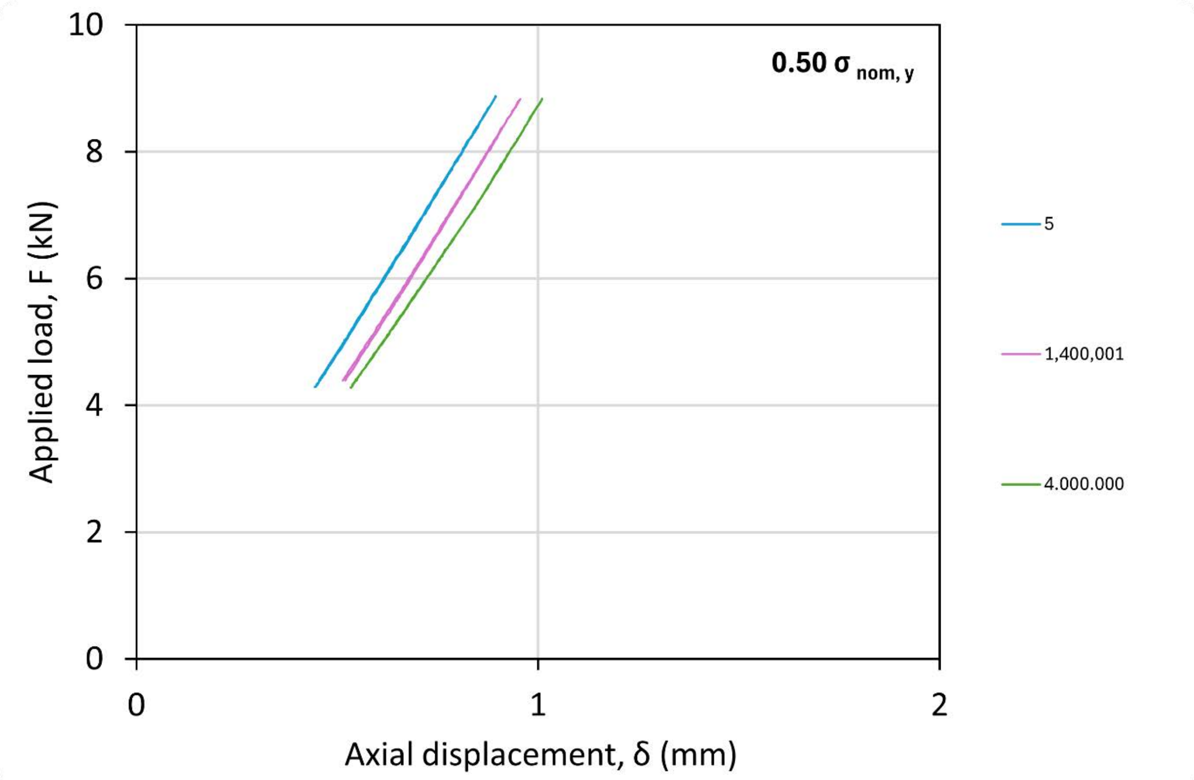

Diagram 5: Load-displacement curves under cyclic loading at specific load stages S355 fillet specimen

1,700,000 cy (a)

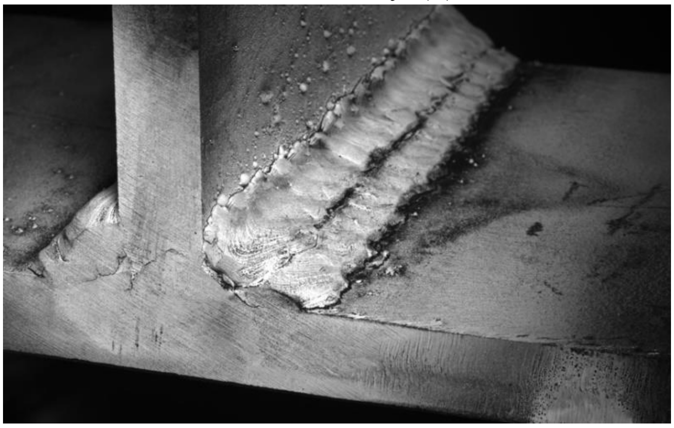

3,000,000 cy (b)

3,000,000 cy
(L-side) (c)

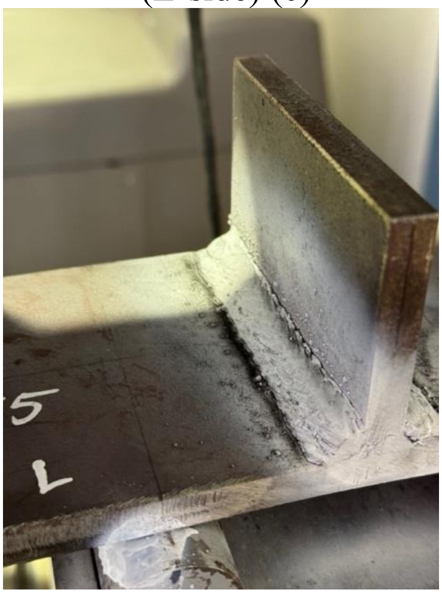

3,000,000
(R-side) (d)

4,000,000
(run out)

R-side (e) L-side (f)

(g)

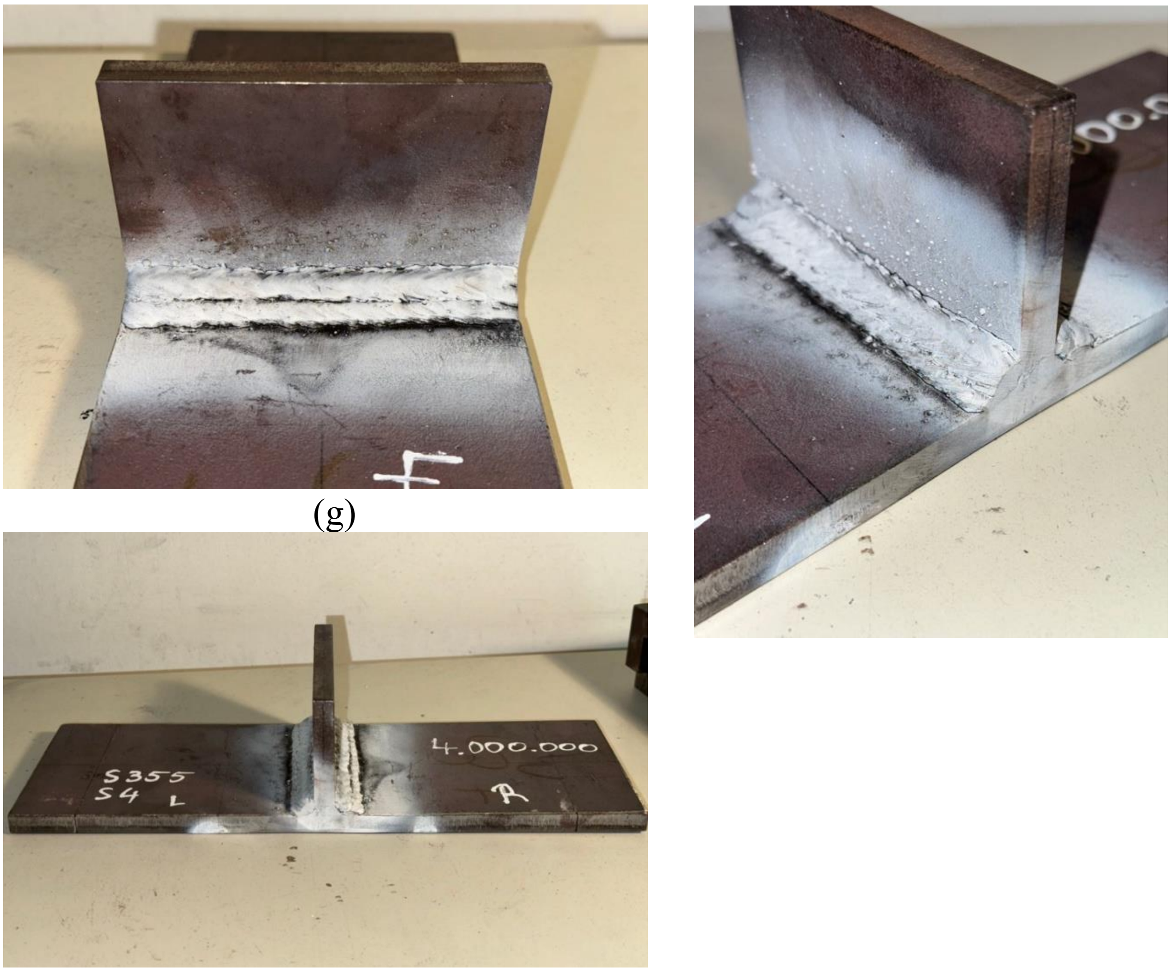

Figure 30: Fatigue crack development at the weld toe for specimen S355_s4_fl under cyclic loading at 50% $\sigma_{nom,\ yield}$ (arrows indicate detected cracks). (a-g)

5.1.2: s700

Sample 1 (91% of $\sigma_{nom,\ max}$):

The following table shows the features of this experiment:

specimen	ΔP (kN)	P_{max} (kN)	$\sigma_{nom,\ max}$ (MPa)	$R = P_{min}/P_{max}$	cycles to failure, n_f
S700_s1_fl	15.8	31.6	640	0.5	87,923

The diagram below describes the behavior of a high-strength steel (HSS) with a yielding stress of 700 Mpa (theoretical value). The most important difference between this and mild steel is that the deviation of the slope does not change significantly until its failure. The material shows a more stable way of behaving and stiffness throughout the whole experiment.

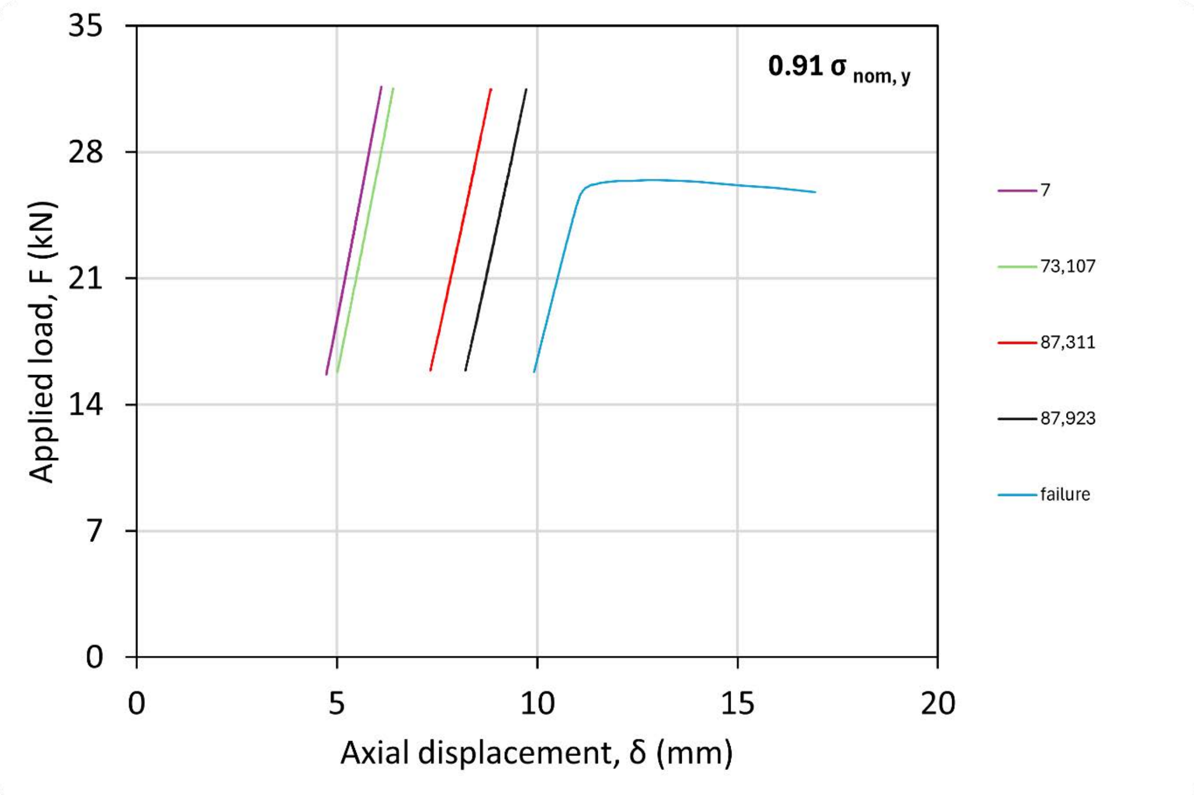

Diagram 6: Load-displacement curves under cyclic loading at specific load stages S700 fillet specimen

It is worth noting that the first crack makes its appearance on the first cycle. More specifically, after reaching the upper limit of load (31.6kn) and completing the first cycle, the process is stopped for the MPI to be applied. As the photos show, the right side of the specimen has a crack, which is a sign that the right side will be the failure side. In the end, the specimen outlasts 87,923 cycles and then collapses.

1st cy.

(a) R-side

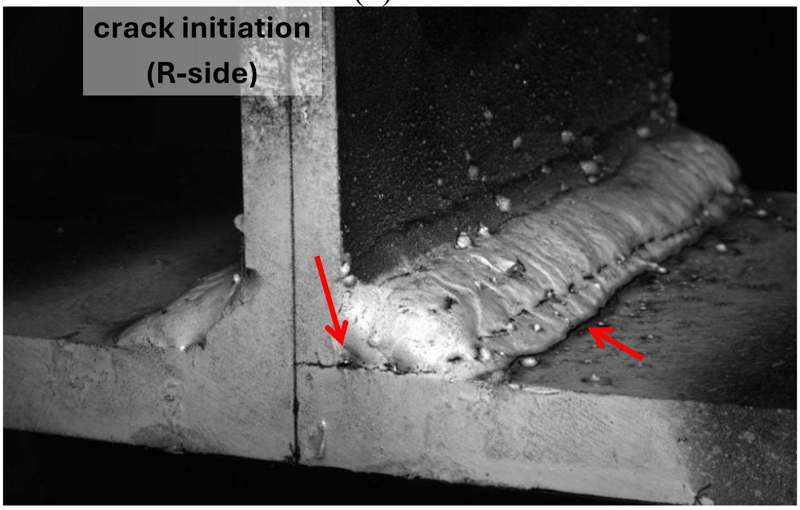

43,600 cy.

(b)L-side

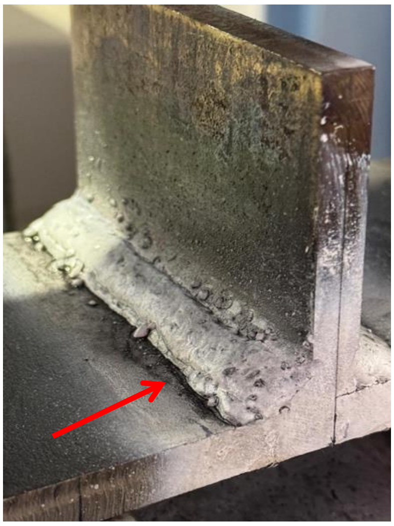

(c)R-side

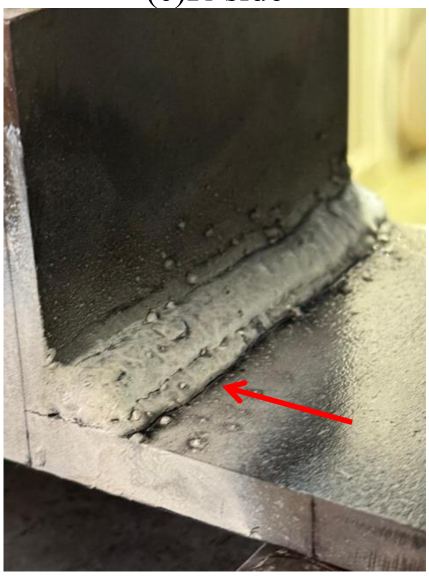

83,000 cy

(d) R-side

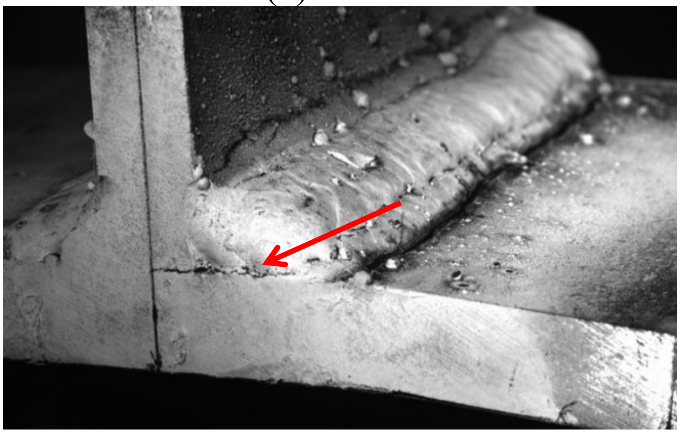

87,923 cy_failure

(e)

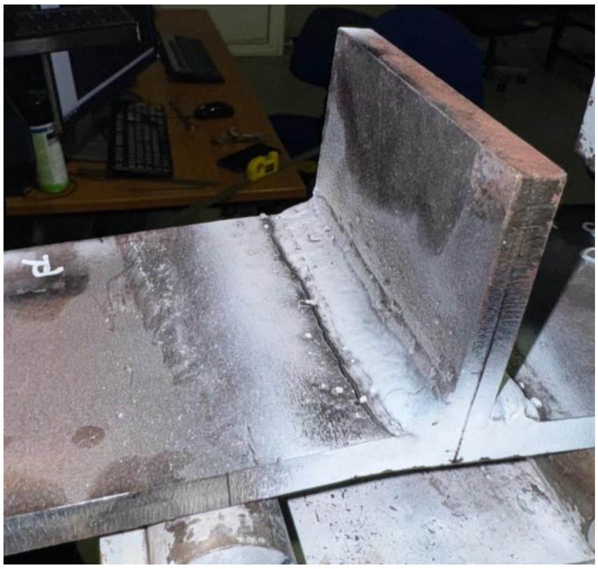

(f)

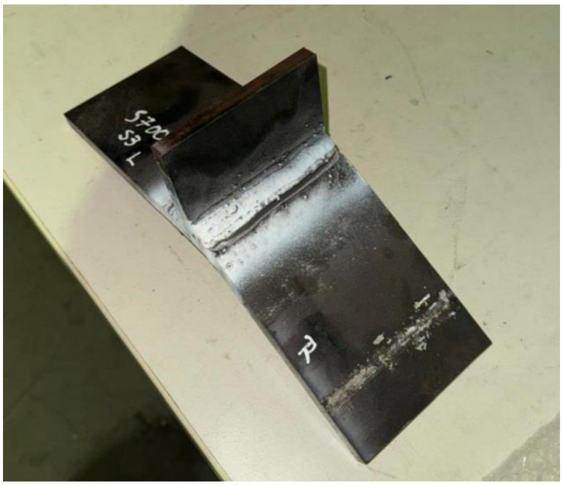

(g)

(h)

Figure 31: Fatigue crack development at the weld toe for specimen S700_s1_fl under cyclic loading at 91% $\sigma_{nom, yield}$ (arrows indicate detected cracks). (a-h)

Sample 2 (75% of $\sigma_{nom, max}$):

The following table shows the features of this experiment:

specimen	ΔP (kN)	P_{max} (kN)	$\sigma_{nom, max}$ (MPa)	$R = P_{min}/P_{max}$	cycles to failure, n_f
S700_s2_fl	12.85	25.7	525	0.5	294,300

Again, it can be easily seen that the s700 HSS has more linear behavior during the procedure.

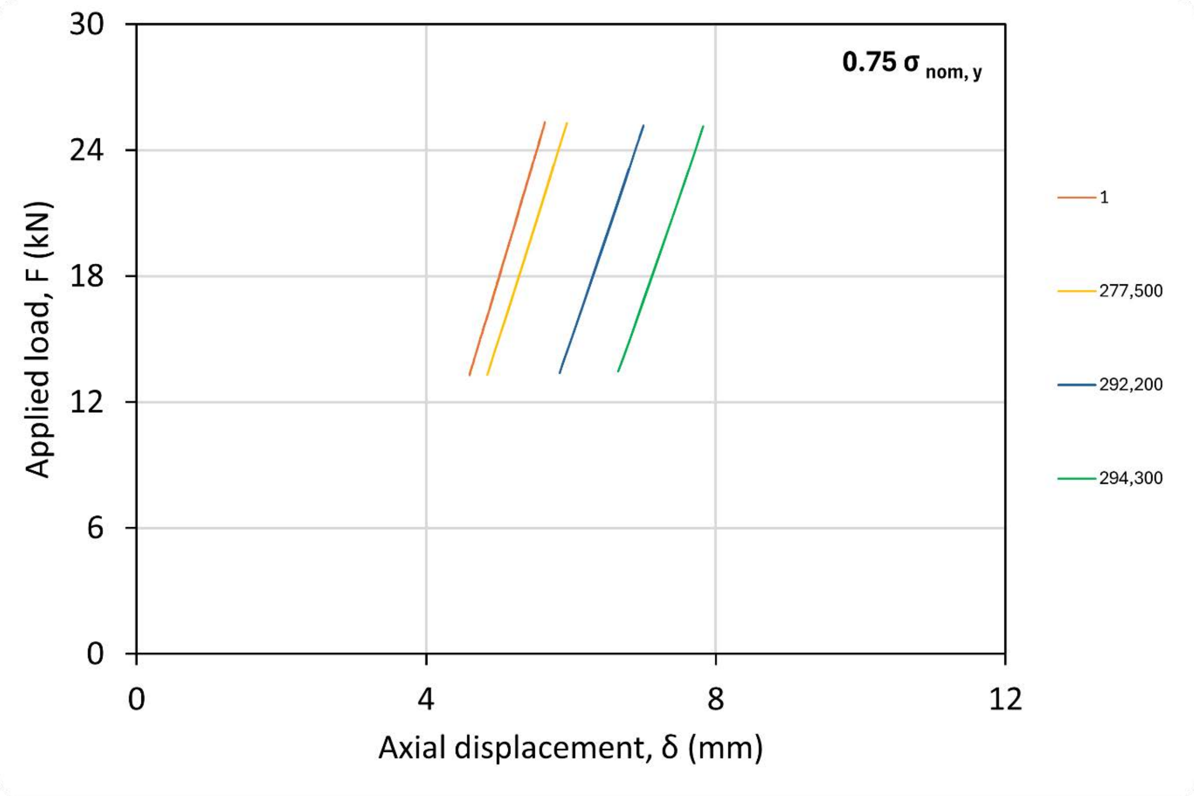

Diagram 7: Load-displacement curves under cyclic loading at specific load stages S700 fillet specimen

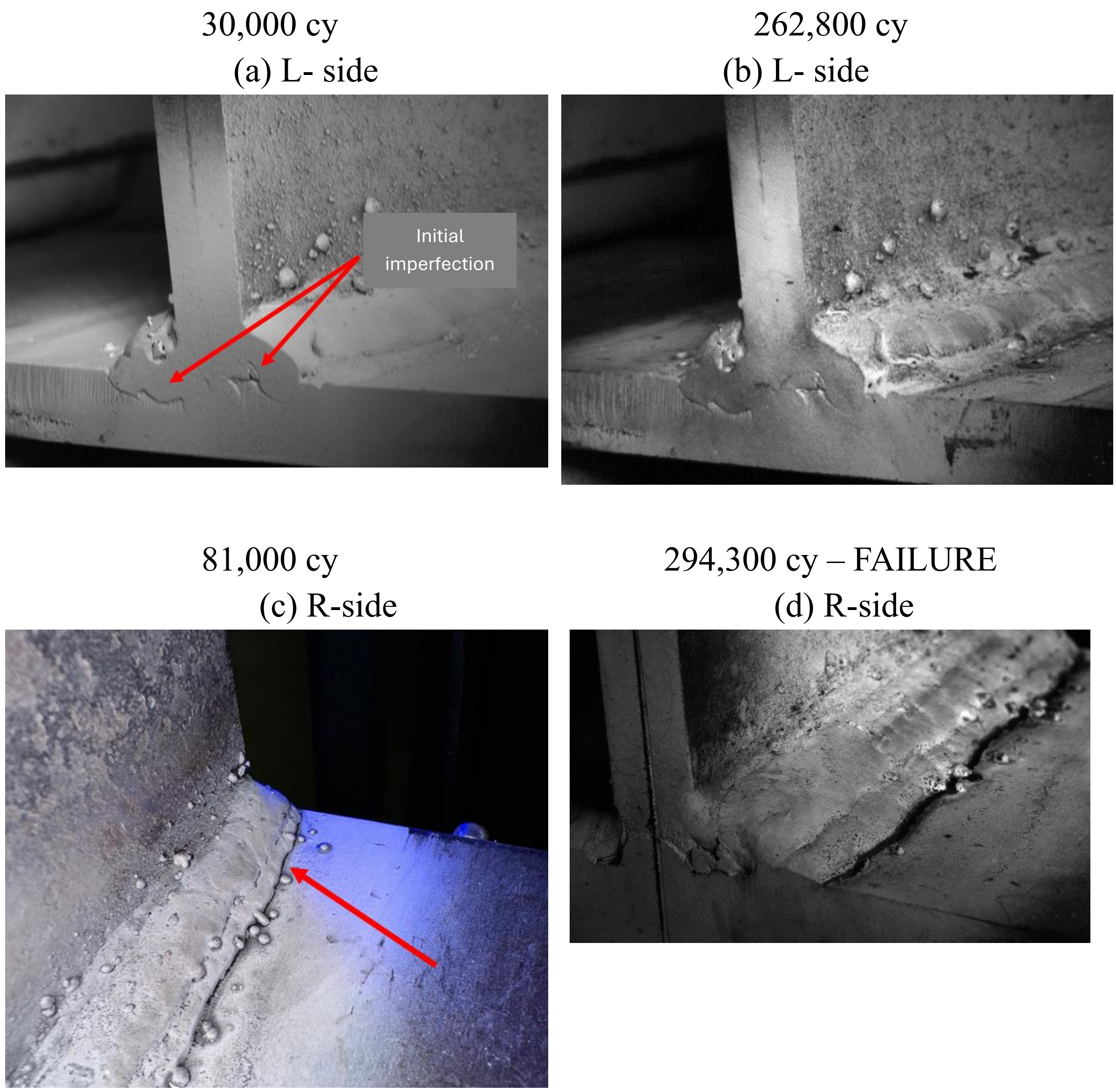

Figure 32: Fatigue crackdevelopment at the weld toe for specimen S700_s2_fl under cyclic loading at 75% $\sigma_{nom, yield}$ (arrows indicate detected cracks). (a-d)

Sample 3 (50% of $\sigma_{nom, max}$):

The following table shows the features of this experiment:

specimen	ΔP (kN)	P_{max} (kN)	$\sigma_{nom, max}$ (MPa)	$R = P_{min}/P_{max}$	cycles to failure, n_f
S700_s3_fl	8.65	17.3	350	0.5	1,143,695

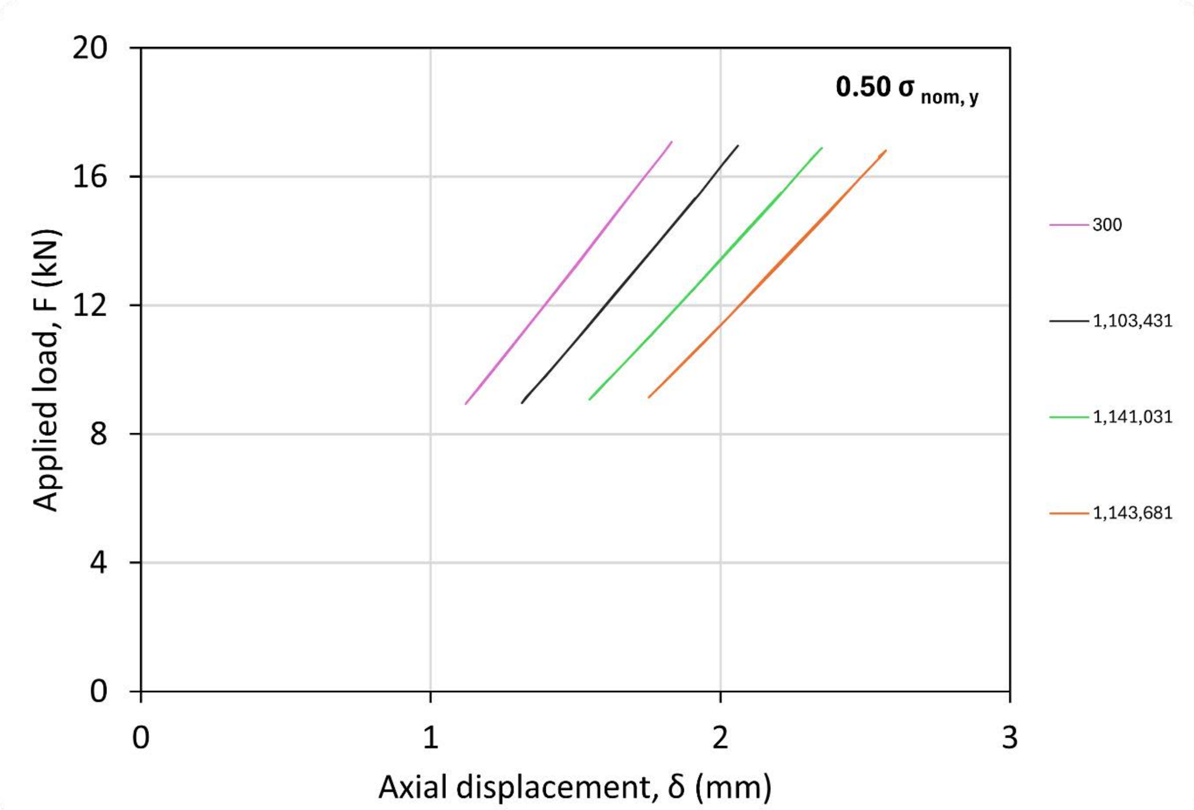

Diagram 8: Load-displacement curves under cyclic loading at specific load stages S700 fillet specimen

21,500 cy

L – side (a)

R – side (b)

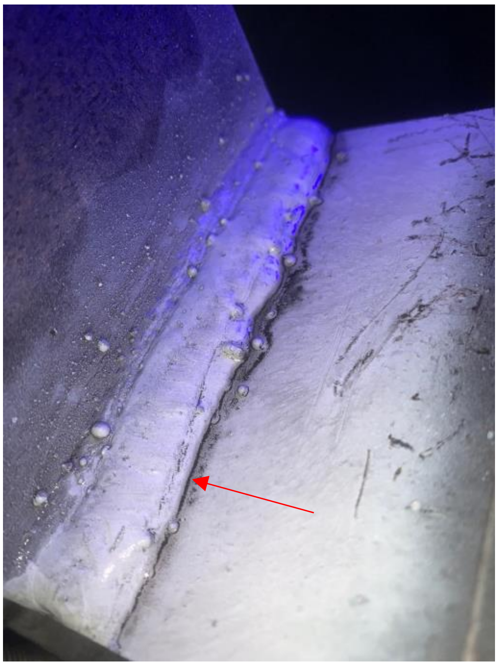

327,000 cy

L – side (c)

R – side (d)

1,136,495 cy

R – side (e)

1,143,695 cy

FAILURE

(f)

(g)

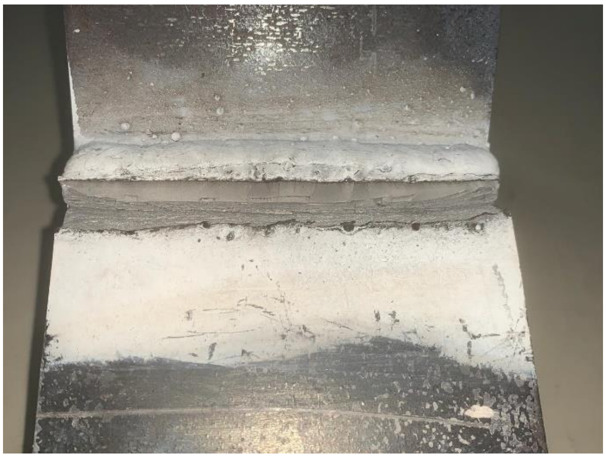

(h)

(i)

Figure 33: Fatigue crack development at the weld toe for specimen S700_s3_fl under cyclic loading at 50% $\sigma_{nom, yield}$ (arrows indicate detected cracks). (a-i)

5.2: Full penetration welded specimens (91%)

5.2.1: s355

The following table shows the features of this experiment:

specimen	ΔP (kN)	P_{max} (kN)	$\sigma_{nom, max}$ (MPa)	$R = P_{min}/P_{max}$	cycles to failure, n_f
S355_s1_fp	8.0	16.0	324	0.5	1,734,000

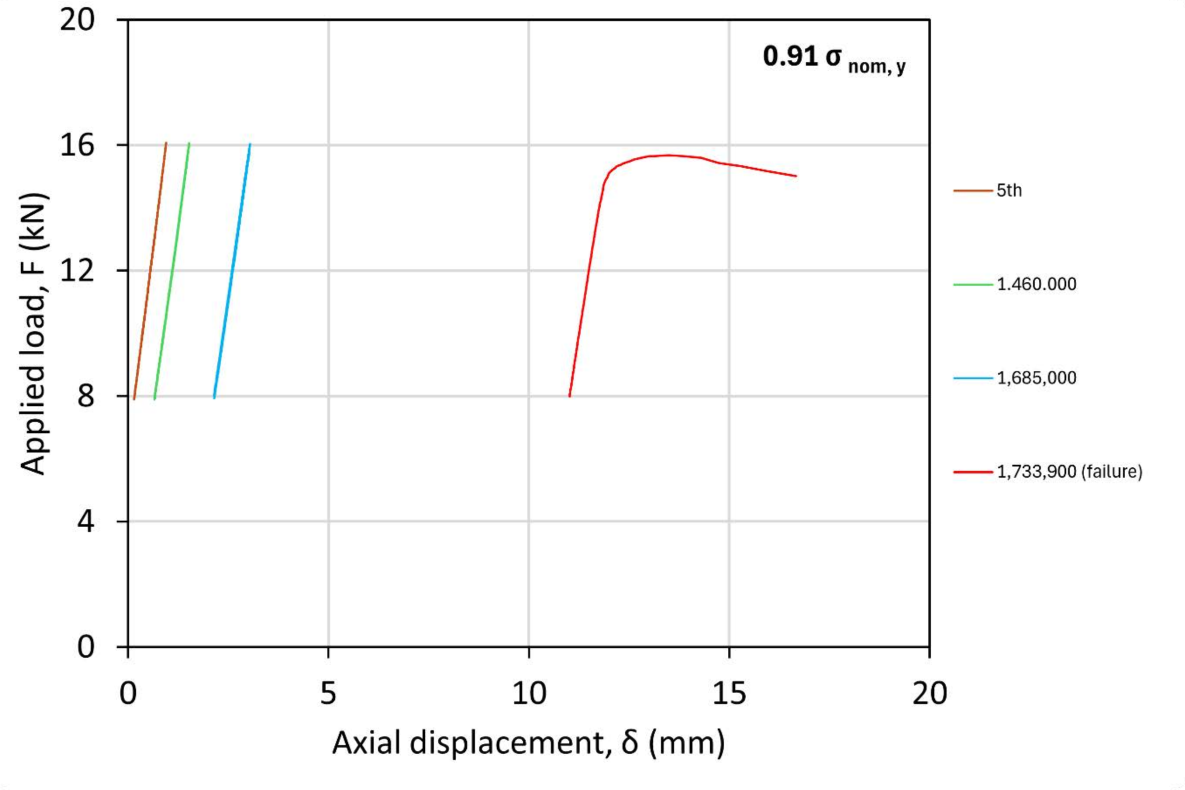

Diagram 9: Load-displacement curves under cyclic loading at specific load stages S355 full penetration specimen

R-side

1 cy (a)

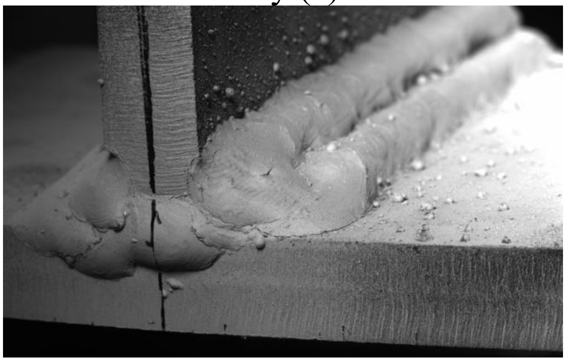

10,000 cy (b)

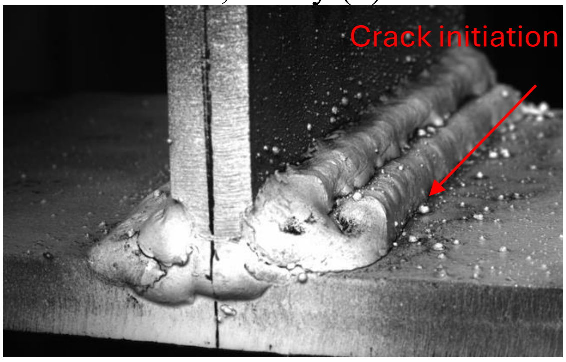

1,720,000 cy (c)

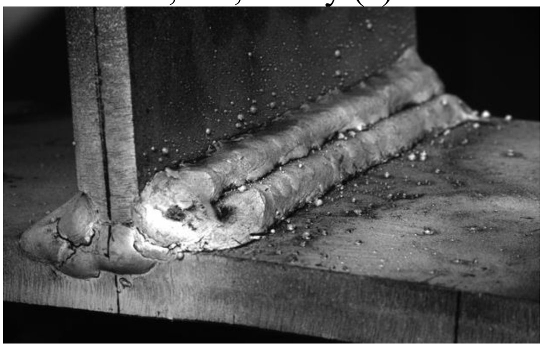

1,733,500 cy (d)

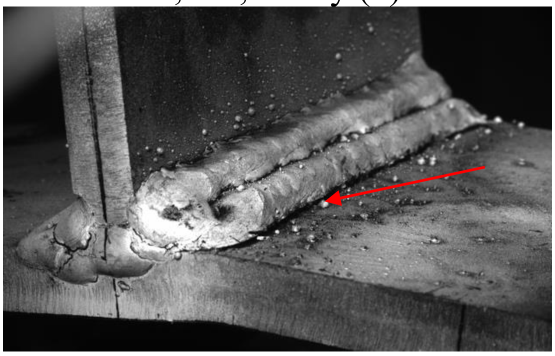

1,733,950 cy (e)

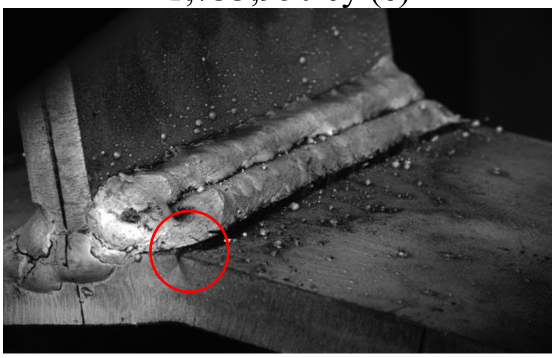

Failure
1,734,000 cy

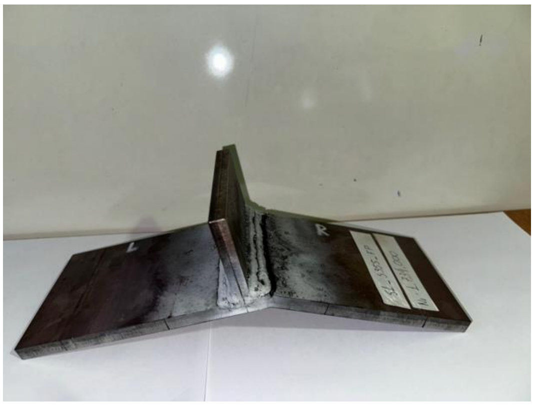

(f)

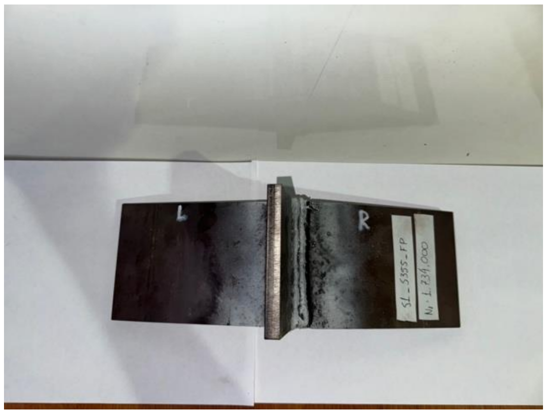

(g)

(h)

Figure 34: Fatigue crack development at the weld toe for specimen S355_s1_fp under cyclic loading at 91% $\sigma_{nom,\ yield}$ (arrows indicate detected cracks). (a-h)

5.2.2: s700

The following table shows the features of this experiment:

specimen	ΔP (kN)	P_{max} (kN)	$\sigma_{nom,\ max}$ (MPa)	$R = P_{min}/P_{max}$	cycles to failure, n_f
S700_s1_fp	15.8	31.6	640	0.5	99,800

This experiment took place in order to make a sufficient comparison between fillet welds and full penetration welds. The expected behavior of the specimen is that it will complete at least the cycles of the fillet welded test and some more. The results were as expected.

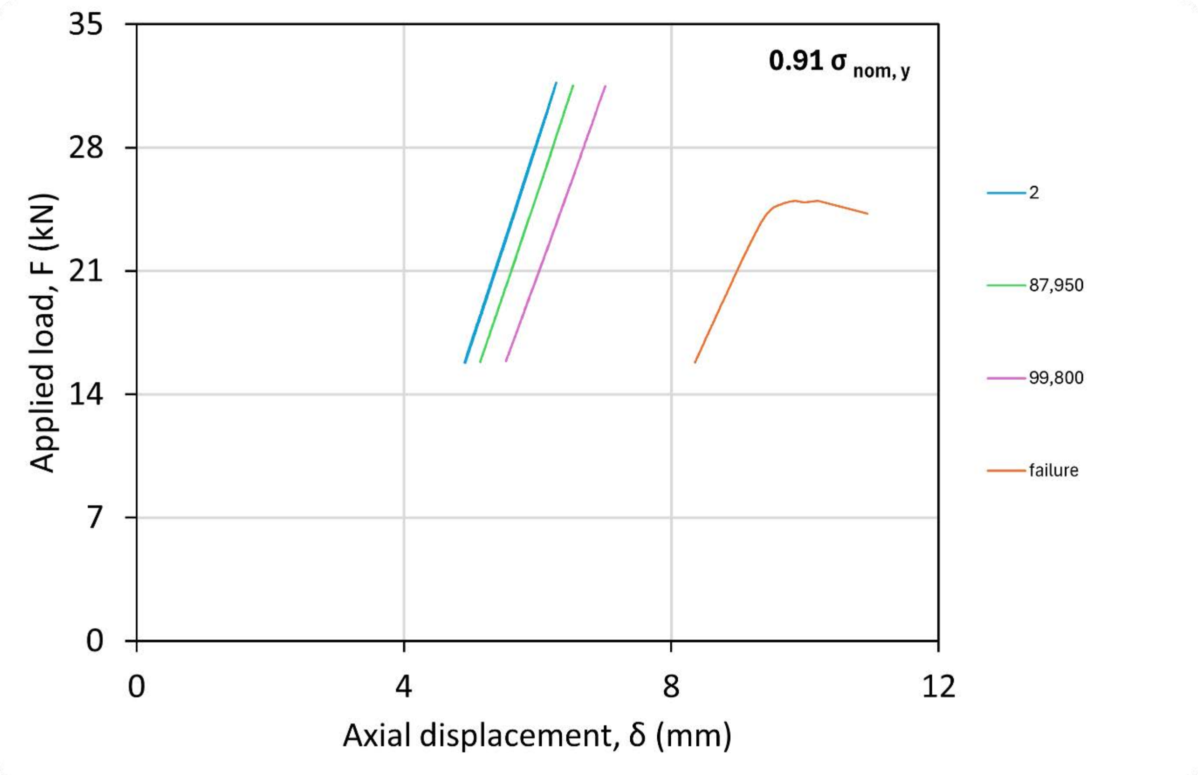

Diagram 10: Load-displacement curves under cyclic loading at specific load stages S700 full penetration specimen

1^{st} cy

L – side (a)

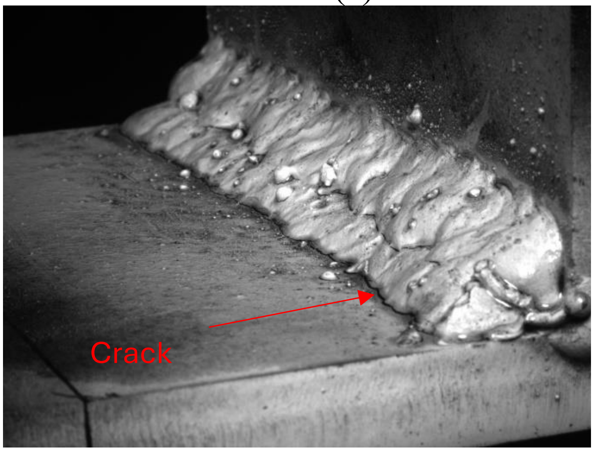

R – side (b)

20,000 cy

L – side (c)

R – side (d)

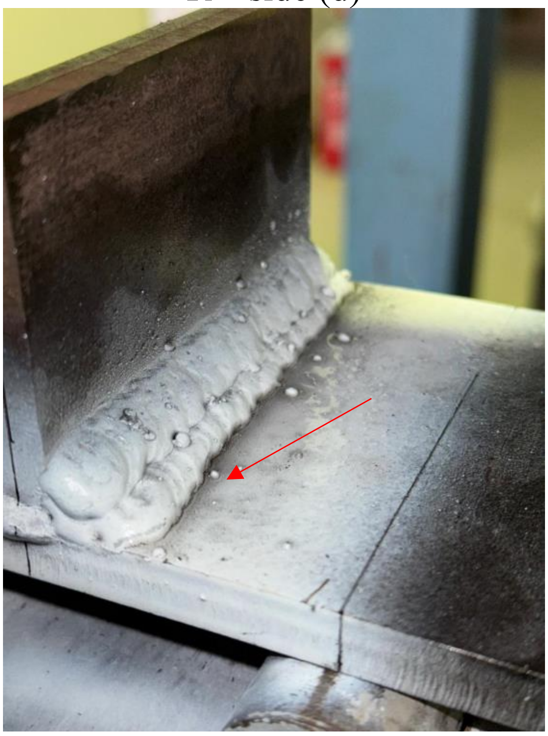

95,200 cy
L – side (e)

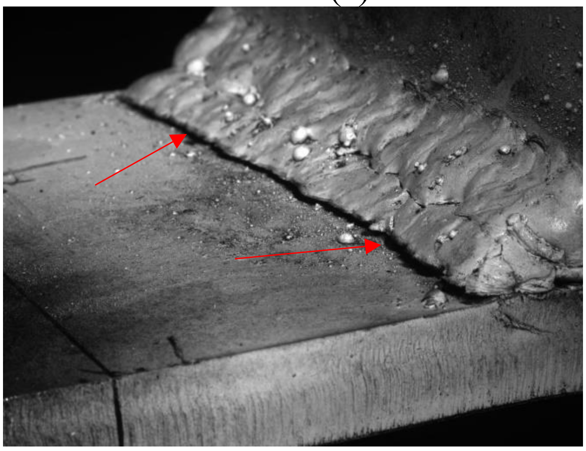

98,200 cy
FAILURE

(f)

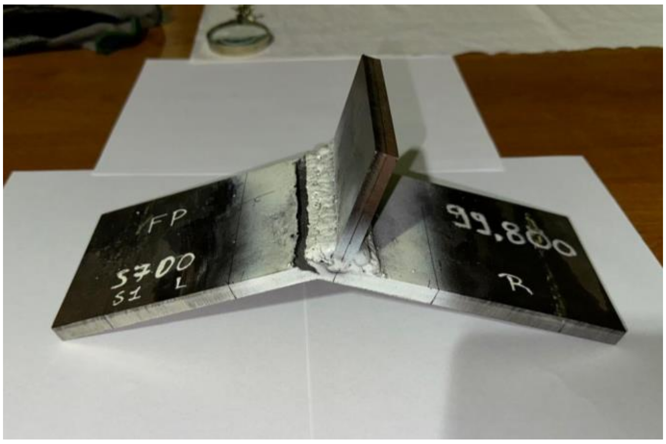

(g)

(h)

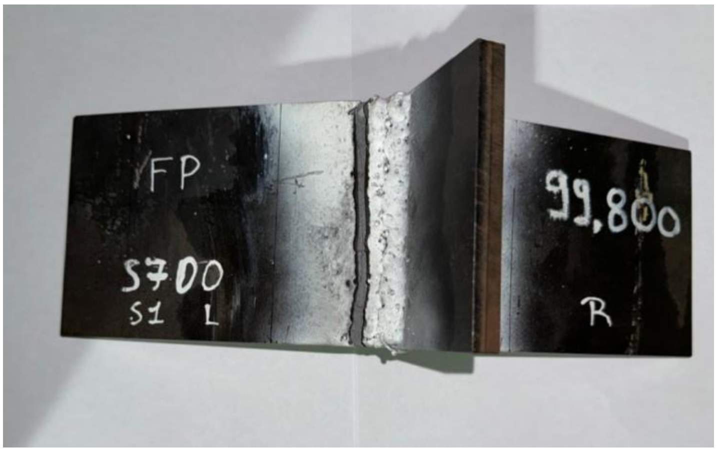

(i)

Figure 35: Fatigue crack development at the weld toe for specimen S700_s1_fp under cyclic loading at 91% $\sigma_{nom, yield}$ (arrows indicate detected cracks). (a-h)

5.3: Full penetration welded specimens with HFMI treatment (91%)

5.3.1: s355

The following table shows the features of this experiment:

specimen	ΔP (kN)	P_{max} (kN)	$\sigma_{nom, max}$ (MPa)	$R = P_{min}/P_{max}$	cycles to failure, n_f
S355_s1_fp_HFMI	8.0	16.0	324	0.5	2,707,600

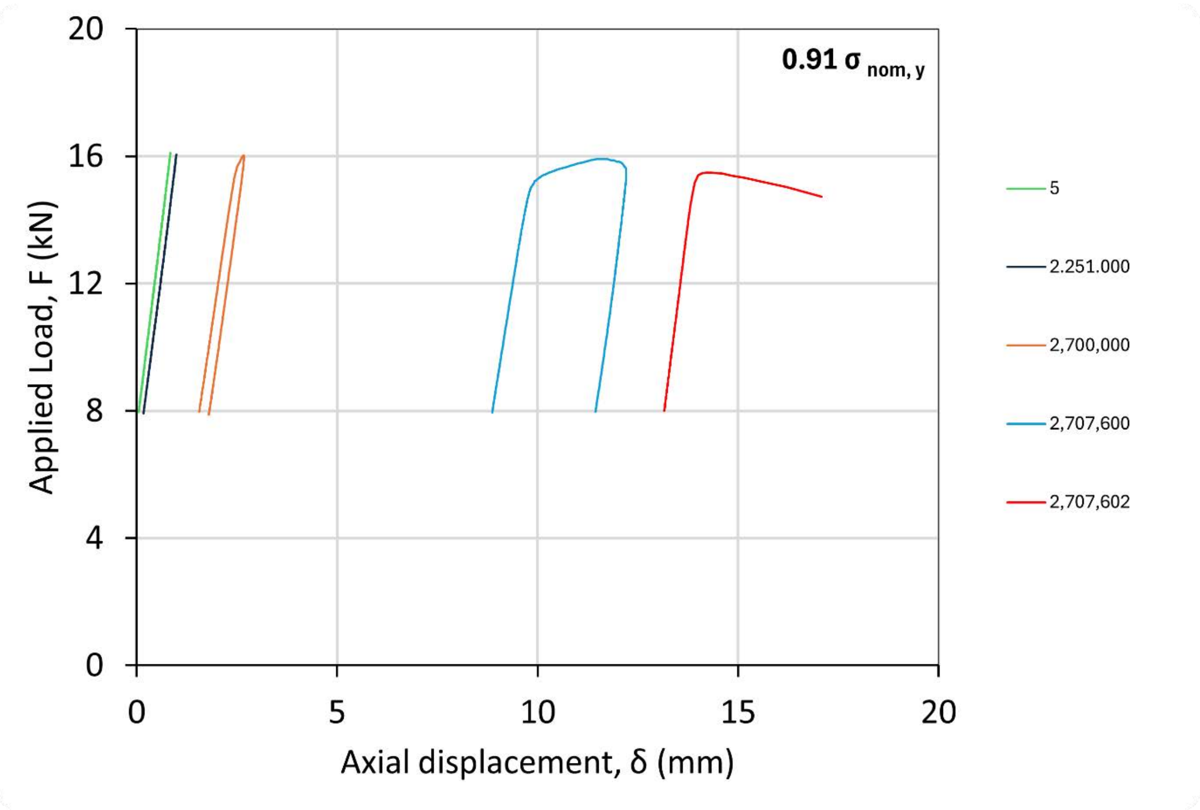

Diagram 11: Load-displacement curves under cyclic loading at specific load stages S355 HFMI specimen

R-side

1 cy (a)

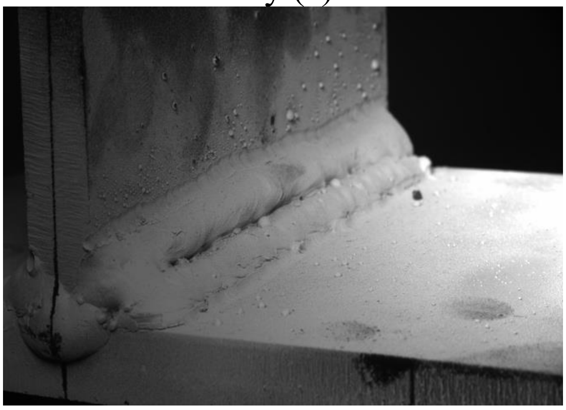

5 cy (b)

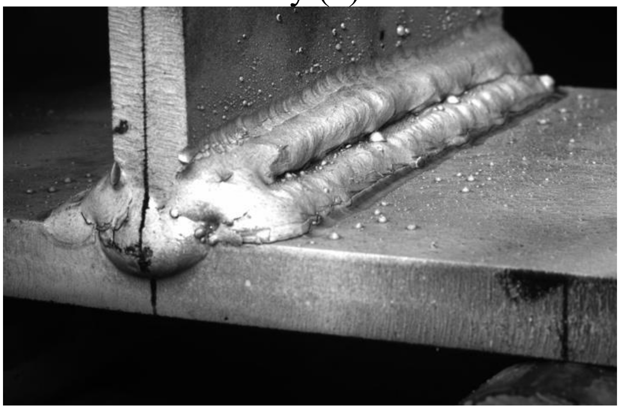

600,000 cy
R-side (c)

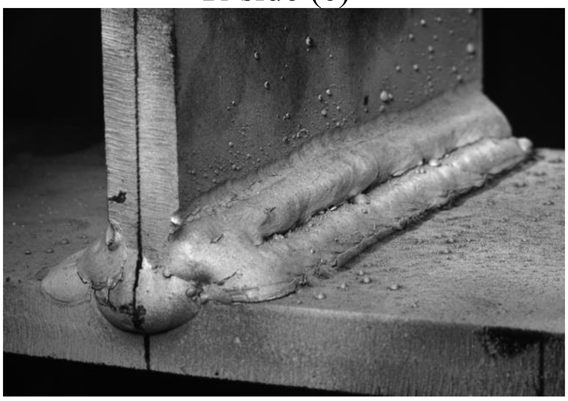

2,700,000 cy
L-side (d)

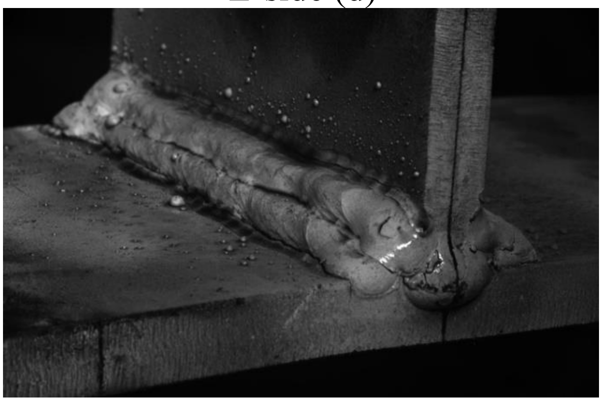

2,705,000 cy
L-side (e)

2,707,600 cy
FAILURE

(f)

(g)

(h)

(i)

Figure 36: Fatigue crack development at the weld toe for specimen S355_s1_fp_HFMI under cyclic loading at 91% $\sigma_{nom, yield}$ (arrows indicate detected cracks). (a-h)

5.3.2: s700

The following table shows the characteristics of this experiment:

specimen	ΔP (kN)	P_{max} (kN)	$\sigma_{nom,\,max}$ (MPa)	$R = P_{min}/P_{max}$	cycles to failure, n_f
S700_s1_fp_HFMI	15.8	31.6	640	0.5	209,070

As explained previously, after a High-Frequency Mechanical Impact process, known as hammer and needle peening, the residual stresses are minimized and, as a result, the material can extend its fatigue resistance from 2 to 10 times. The diagram below presents exactly that behavior.

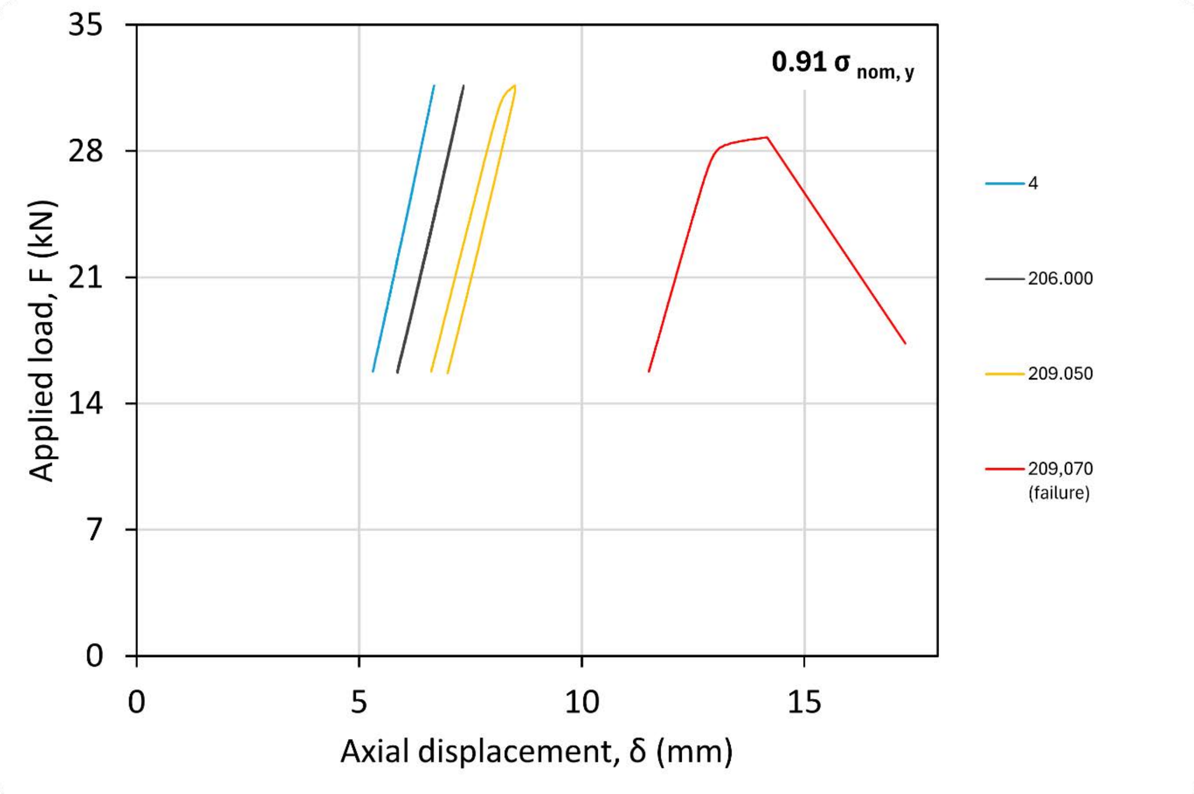

Diagram 12: Load-displacement curves under cyclic loading at specific load stages S700 HFMI specimen

Crack initiation on the left side takes place in the 5th cycle, as on the right side the rupture occurs in the 100th cycle.

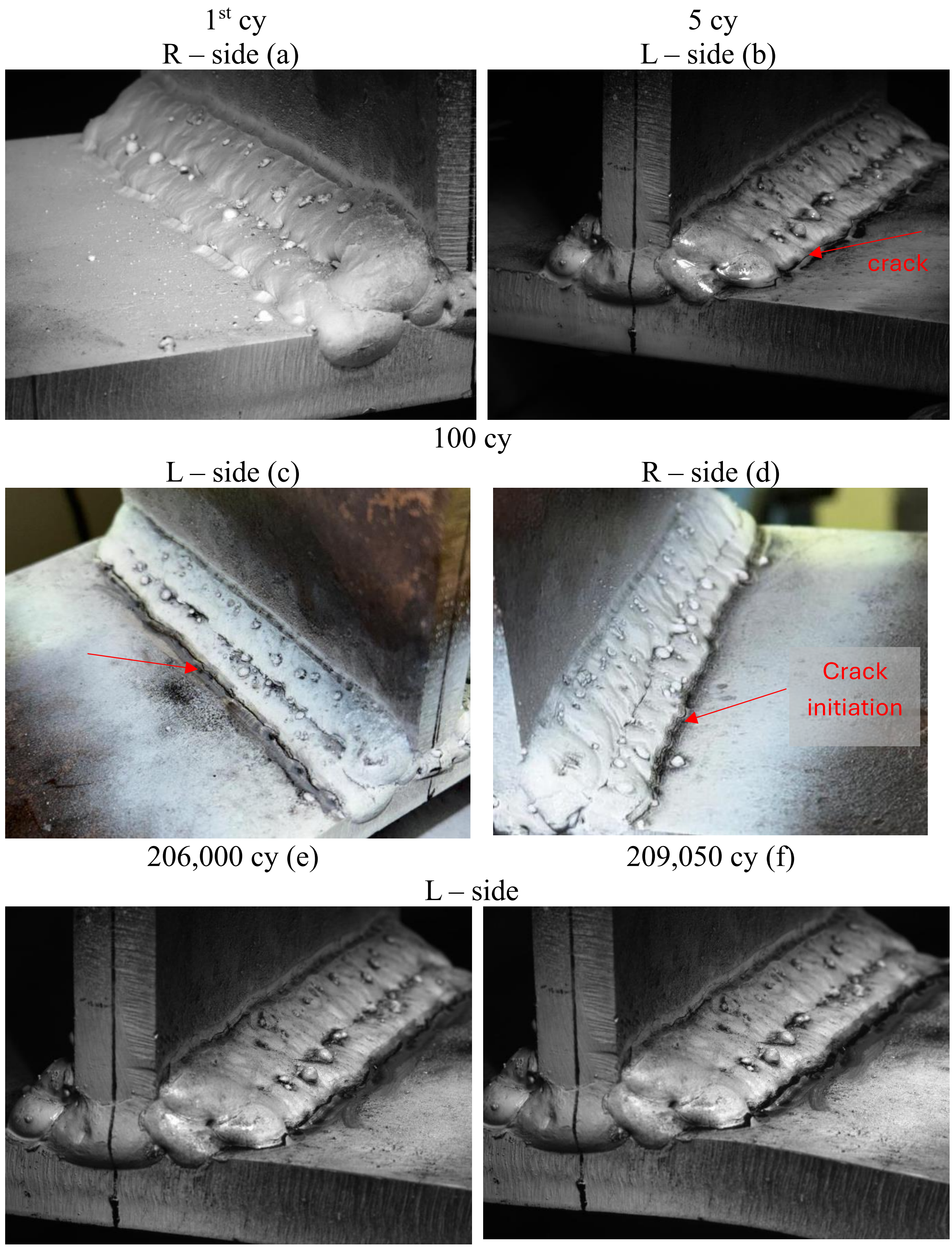
1st cy
R – side (a)
5 cy
L – side (b)
crack
100 cy
L – side (c)
R – side (d)
Crack
initiation
206,000 cy (e)
209,050 cy (f)
L – side

209,070 cy
FAILURE

(g)

(h)

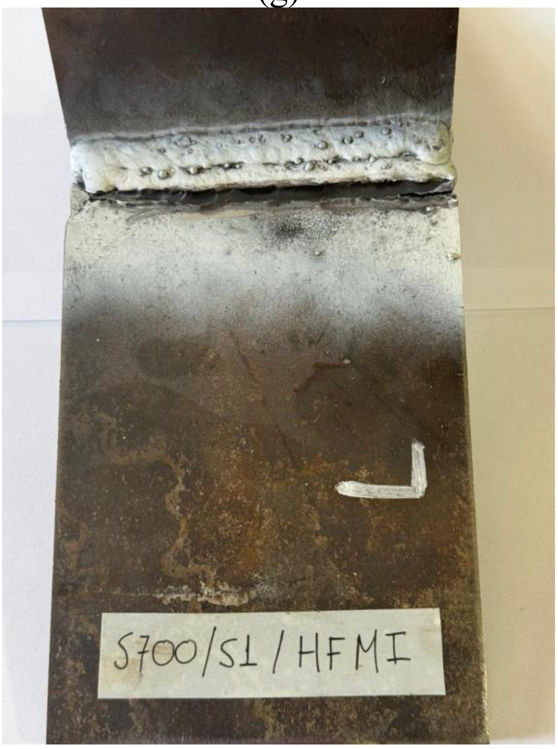

(i)

Figure 37: Fatigue crack development at the weld toe for specimen S700_s1_fp_HFMI under cyclic loading at 91% $\sigma_{nom, yield}$ (arrows indicate detected cracks). (a-i)

Stiffness comparison

Stiffness refers to the ability of specimens to resist deformation when subjected to external forces. It measures the amount applied load required to cause a certain amount of deflection in the specimen. In practical terms, stiffness represents the ability of the specimen to withstand bending without significant loss of its original shape. As shown in diagram 13, when comparing the fifth cycle of each specimen at the highest tested amplitude (91% $\sigma_{nom, yield)}$) where the behavior is linear, its observed that stiffens is identical, regardless of the material, welding type, or treatment procedure. [13]

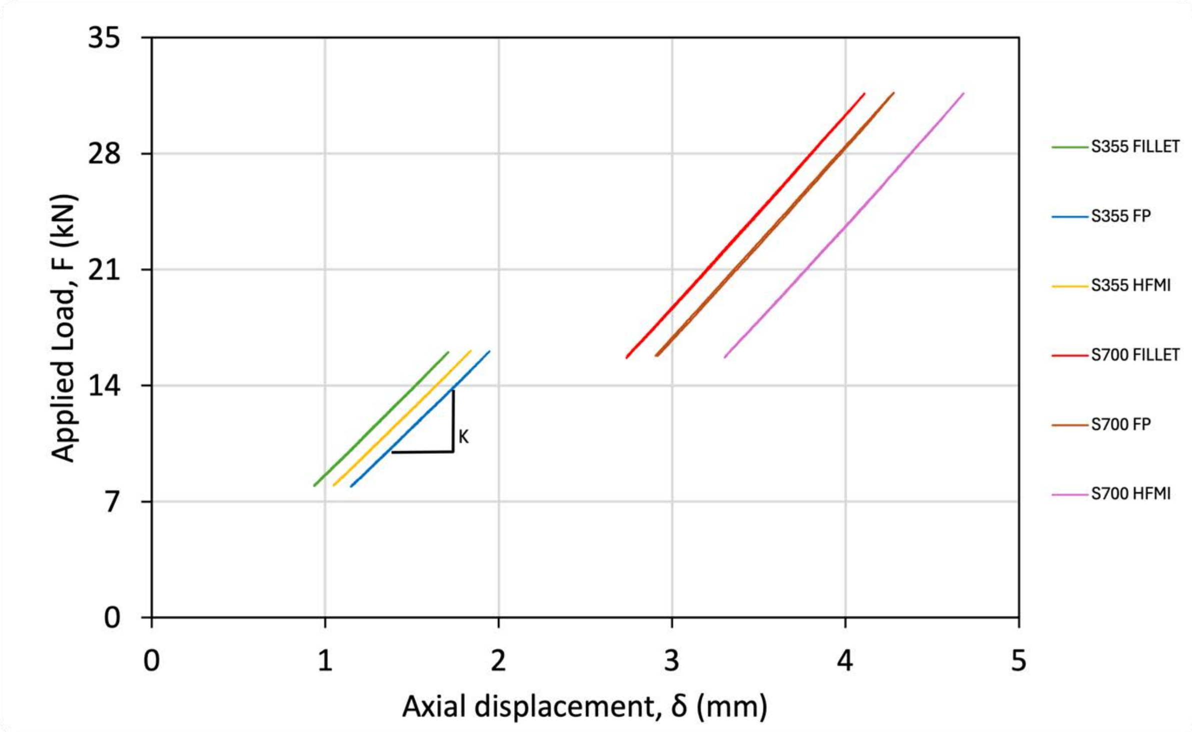

Diagram 13: stiffness comparison at the fifth cycle of all the specimens at 91% $\sigma_{nom, yield}$

Chapter 6: Conclusion and Summary

This dissertation contributes to the development of the current state-of-art towards renewable TLP (REFOS). This platform is defined by cost-effectiveness and structural integrity. An overview is developed with significant data on cycles to failure, crack initiation, failure modes and locations, and change in stiffness during the cyclic loading as a result of four-point-bending high-cycle fatigue. Key observations from the conducted experiments are outlined below:

- The location of crack initiation and failure (weld toe) were consistent across all specimens

- In all steel grades and welding types, as the amplitude increased the cycles to failure decreased as expected

- S355 specimens showed superior fatigue resistance compered to S700 when tested at the same percentage of nominal yielding stress for each steel grade

- As indicated by material properties, mild steel S355 is more ductile than S700 high-strength steel. As a result, S355 specimens have a more predictable and linear behavior

- S355specimens with full penetration welds showed a 58% increase in fatigue performance compared to S355 with fillet welds at the highest amplitude (0.91 $\sigma_{nom, y}$) tested. In contrast, S700 specimens with full penetration welds showed a 14% increase in fatigue performance compared to S700 specimens with fillet welds on the highest amplitude (0.91 $\sigma_{nom, y}$)

- High Frequency Mechanical Impact (HFMI) treatment increases the fatigue life of S355 full penetration specimens by 56%, and S700 full penetration specimens by 110% at the highest amplitude tested (0.91 $\sigma_{nom, y}$)

- The initial stiffness of all specimens is identical and no significant reduction was observed throughout the experiments

The experiments were conducted in room conditions to set the basis for optimizing the concept of SIRENES. Widening the experiments in corrosive environment (seawater) and redesigning the TLP platform (REFOS) accordingly. Reviewing the stress-critical areas, working with different steel grades and analyzing their behavior under external load to simulate extreme environmental conditions will ensure the required structural integrity and cost efficiency, while enhancing their competitiveness in the international energy sector.

6.1 Future work

As the current thesis concludes its investigation into the fatigue examination of high-strength steel, several avenues for future research and development merit attention. The findings from this study serve as a stepping stone for further exploration and enhancement of offshore wind turbine components. Some brief suggestions for further investigation include:

- Fatigue testing of welded components (fillet-welded T-joints and full-penetration T-joints) under corrosive environment.
- Fractographic examination of failed specimens.
- Fatigue simulations using advanced Numerical methods and FE models.
- Expand the examination using other steel grades.

REFERENCES

1.Wikipedia contributors. (2024, January 19). *Floating wind turbine*. Wikipedia. https://en.wikipedia.org/wiki/Floating_wind_turbine

2.Deliverable D1.1-REFOS, 2017: State-of-the-art-review

3. Deliverable D1.1-SIRENES, 2020: Proposal motivation and objectives

4. Deliverable D1.3-SIRENES, 2020: Scientific methodology

5. Deliverable D1.2-SIRENES, 2020: Challenges and state-of-the-art

6. Ultimate strength and fatigue of stiffened welded tubular joints in floating energy production structures, Theocharis Papatheocharis, George T. Plakias, Anna D. Zervaki, Philip C. Perdikaris, Spyros A. Karamanos

7. Mechanical behavior of material, 2021, Spiros G. Padelakis, Konstantinos I. Tserpes, Tziola

8. Fracture and fatigue of s355 and s700 steel for floating wind energy structures, Lachanidis Vasileios, Ntakis Vasileios, University of Thessaly

9. Mechanics of Materials, book II, Professor Aravas Nikos, University of Thessaly

10. https://www.structuralbasics.com/fillet-weld/

11. https://sonats-et.com/en/hfmi-treatment/ultrasonic-impact-treatment/

12. https://thegraduateengineer.com/what-is-mpi-magnetic-particle-inspection/

13. https://www.ssab.com/en-ca/support/how-to-design/general-design/20-questions-about-structural-stiffness